Cancer Cell

Article

Fibrotic response to anti-CSF-1R therapy potentiates glioblastoma recurrence

Graphical abstract

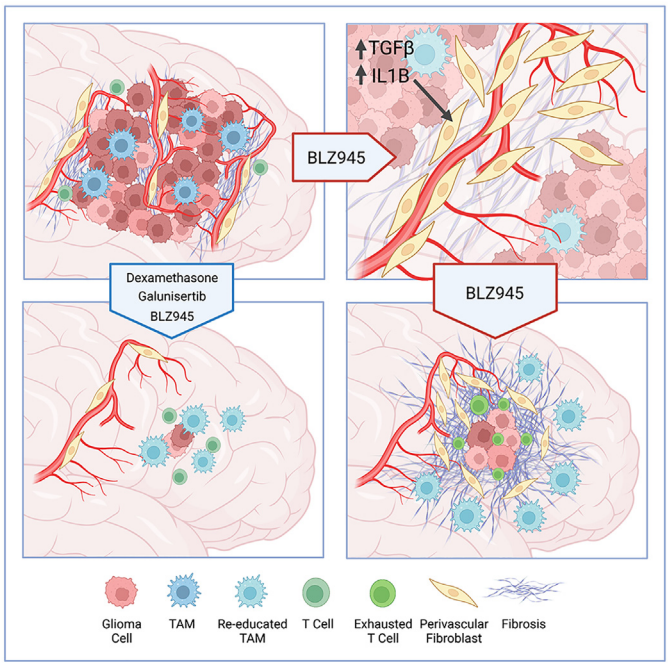

Authors

Spencer S. Watson, Anoek Zomer, Nadine Fournier, ..., Giulia Cossu, Andreas F. Hottinger, Johanna A. Joyce

Correspondence

johanna.joyce@unil.ch

In brief

Watson et al. show that multiple modes of therapy-induced glioblastoma regression are associated with fibrosis, which promotes tumor cell survival. Using multi-omics analyses, they identify the signaling pathways related to immunotherapy-associated fibrosis and show that inhibition of this response improves survival in preclinical trials.

Highlights

- Multi-omics profiling of the glioblastoma TME following immunotherapy treatment
- Multiple modes of glioblastoma therapy trigger a fibrotic response
- Post-treatment fibrotic niches promote tumor cell survival and recurrence
- Inhibition of treatment-associated fibrosis improves efficacy of anti-CSF-1R therapy

Watson et al., 2024, Cancer Cell *42*, 1507–1527
September 9, 2024
https://doi.org/10.1016/j.ccell.2024.08.012

CellPress

Cancer Cell

CellPress
OPEN ACCESS

Article

Fibrotic response to anti-CSF-1R therapy potentiates glioblastoma recurrence

Spencer S. Watson,[1,2,3,4,5,17] Anoek Zomer,[1,2,3,4,17] Nadine Fournier,[4,6] Joao Lourenco,[4,6] Manfredo Quadroni,[7] Agnieszka Chryplewicz,[4,8] Sina Nassiri,[4,6] Pauline Aubel,[1,2,3,4,5] Simona Avanthay,[1,2,3,4] Davide Croci,[1,2,3,4] Erik Abels,[9,10] Marike L.D. Broekman,[9,10] Douglas Hanahan,[1,2,3,4,8,11] Jason T. Huse,[12,13] Roy T. Daniel,[5,14] Monika E. Hegi,[5,15] Krisztian Homicsko,[1,2,3,4,16] Giulia Cossu,[5,12,13] Andreas F. Hottinger,[1,2,3,4,5,16] and Johanna A. Joyce[1,2,3,4,5,11,18,*]

[1]Department of Oncology, University of Lausanne, 1011 Lausanne, Switzerland
[2]Ludwig Institute for Cancer Research, University of Lausanne, 1011 Lausanne, Switzerland
[3]Agora Cancer Research Center Lausanne, 1011 Lausanne, Switzerland
[4]Agora Cancer Centre, University Hospital Lausanne, 1011 Lausanne, Switzerland
[5]Lundin Brain Tumour Centre, University Hospital Lausanne, 1011 Lausanne, Switzerland
[6]Translational Data Science Facility, SIB Swiss Institute of Bioinformatics, Agora Cancer Research Center Lausanne, 1011 Lausanne, Switzerland
[7]Proteomics Core Facility, University of Lausanne, 1011 Lausanne, Switzerland
[8]Swiss Institute for Experimental Cancer Research (ISREC), School of Life Sciences, Swiss Federal Institute of Technology Lausanne (EPFL), Lausanne, Switzerland
[9]Department of Neurosurgery, Department of Cell and Chemical Biology, Leiden University Medical Center, 2300 RC Leiden, the Netherlands
[10]Department of Neurosurgery, Haaglanden Medical Center, 2597 The Hague, the Netherlands
[11]Swiss Cancer Center Leman (SCCL), Lausanne, Geneva, Switzerland
[12]Department of Pathology, University of Texas MD Anderson Cancer Center, Houston, TX 77030, USA
[13]Department of Translational Molecular Pathology, University of Texas MD Anderson Cancer Center, Houston, TX 77030, USA
[14]Department of Neurosurgery, University Hospital of Lausanne, 1011 Lausanne, Switzerland
[15]Department of Clinical Neurosciences, University Hospital Lausanne, 1011 Lausanne, Switzerland
[16]Department of Oncology, University Hospital of Lausanne, 1011 Lausanne, Switzerland
[17]These authors contributed equally
[18]Lead contact
*Correspondence: johanna.joyce@unil.ch
https://doi.org/10.1016/j.ccell.2024.08.012

SUMMARY

Glioblastoma recurrence is currently inevitable despite extensive standard-of-care treatment. In preclinical studies, an alternative strategy of targeting tumor-associated macrophages and microglia through CSF-1R inhibition was previously found to regress established tumors and significantly increase overall survival. However, recurrences developed in ~50% of mice in long-term studies, which were consistently associated with fibrotic scars. This fibrotic response is observed following multiple anti-glioma therapies in different preclinical models herein and in patient recurrence samples. Multi-omics analyses of the post-treatment tumor microenvironment identified fibrotic areas as pro-tumor survival niches that encapsulated surviving glioma cells, promoted dormancy, and inhibited immune surveillance. The fibrotic treatment response was mediated by perivascular-derived fibroblast-like cells via activation by transforming growth factor β (TGF-β) signaling and neuroinflammation. Concordantly, combinatorial inhibition of these pathways inhibited treatment-associated fibrosis, and significantly improved survival in preclinical trials of anti-colony-stimulating factor-1 receptor (CSF-1R) therapy.

INTRODUCTION

Glioblastoma is the most common primary brain tumor in adults.[1] Standard-of-care (SoC) treatment for these high-grade gliomas includes surgery, temozolomide-based chemotherapy, and fractionated ionizing radiation (IR). However, despite SoC treatment, the median survival for patients is just over 14 months following diagnosis, and the 5-year survival rate is less than 5%.[1,2] Nearly all glioblastomas eventually recur following treatment, underscoring the need to better understand therapeutic resistance mechanisms.

One of the major challenges in developing effective therapies for glioblastoma is the high degree of genomic instability and cellular plasticity, resulting in extensive intratumoral heterogeneity and therapy-resistant subclones.[3,4] A promising alternative strategy is to target components of the more genomically

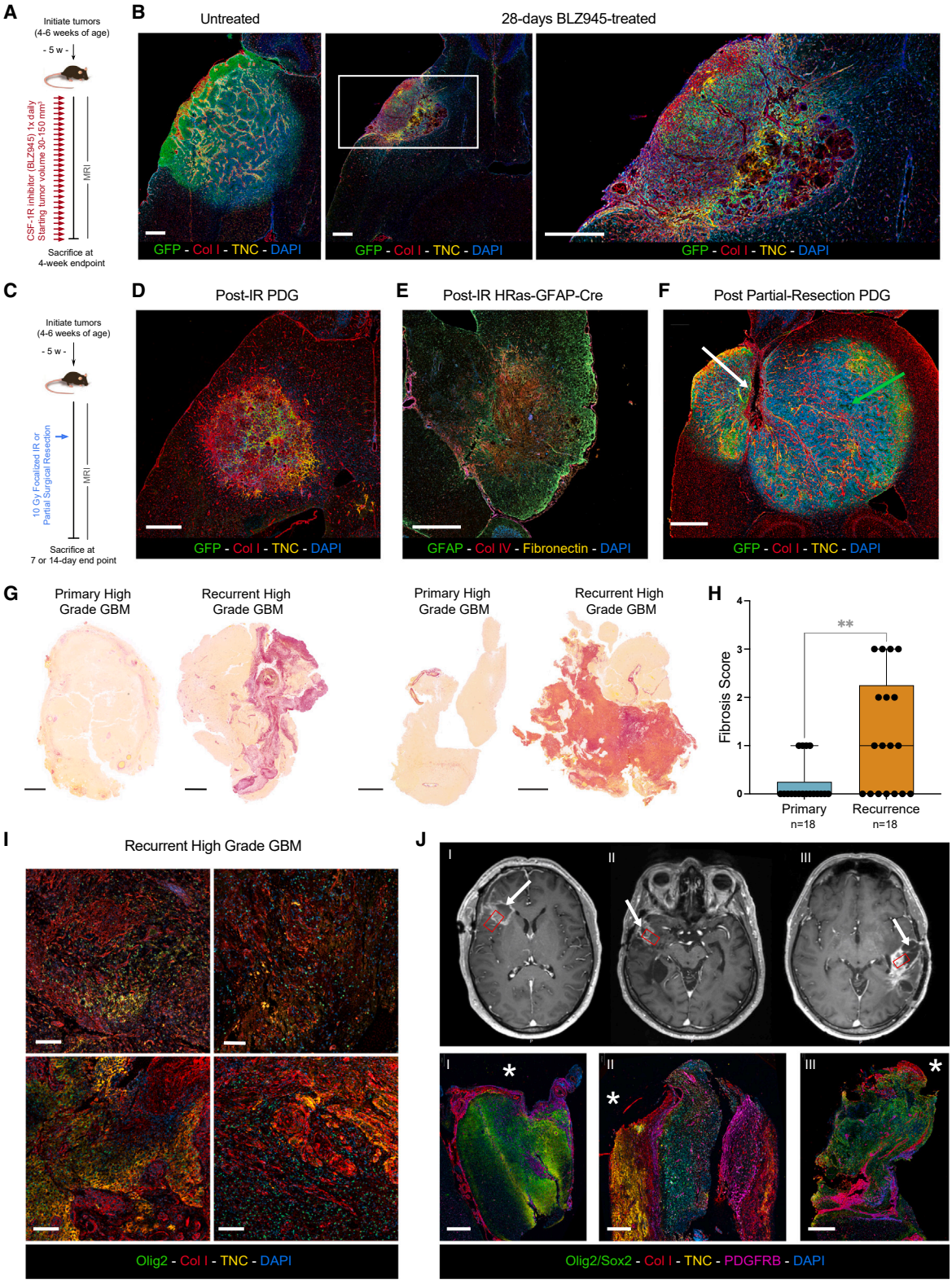

Figure 1. Multiple treatment modalities trigger a fibrotic response in glioblastoma

(A) Schematic of preclinical treatment regimen for the murine model of PDGFB-driven glioblastoma.

(B) Representative IF images of tumors prior to treatment (left panel) and following 28 days of BLZ945 treatment (middle panel, area enlarged in right panel). Tumor cells labeled with GFP, fibrosis labeled with Col I and TNC. Scale bars: 500 μm.

(legend continued on next page)

stable tumor microenvironment (TME). Previously, we found that tumor-associated macrophages and microglia (TAMs) constitute the largest population of the glioblastoma immune microenvironment in patients.[5] Additionally, since elevated numbers of TAMs are associated with high tumor grade and poor patient prognosis in many cancers, including gliomas,[6–8] we have previously investigated the potential of therapeutically targeting TAMs by blocking signaling of the colony-stimulating factor-1 receptor (CSF-1R).[9] In multiple models, we found that CSF-1R inhibition re-educated TAMs, substantially regressed established high-grade gliomas, and markedly increased survival in preclinical trials.[10–13] While overall survival was significantly prolonged in response to CSF-1R inhibition, tumors eventually recurred in ~50% of mice throughout these long-term experiments.[10] Interestingly, histological analyses revealed that 100% of recurrent tumors regrew immediately adjacent to regions of glial scarring.[10] By contrast, scars were only observed in ~20% of the treated mice surviving to the trial endpoint, suggesting a potential mechanistic link between scarring and glioma recurrence.

Scarring in the central nervous system (CNS) in other contexts has been shown to involve multiple cell-signaling cascades initiated by physical damage, inflammation, or oxygen deprivation.[14] The function of CNS scarring is to circumscribe the lesion site, thereby containing CNS damage, inhibiting excessive immune-mediated death of cells surrounding the lesion, and allowing for axonal regrowth to restore neurological function. However, in the context of glioblastoma, these same functions could have protective and even tumor-promoting effects. More generally, fibrosis in extracranial cancers has been reported to have pro- or anti-tumoral functions depending on the context.[15–17] For example, in early-stage tumors, a fibrotic response can slow growth and impede local invasion, but as tumors progress, increased stiffness and re-organization of the extracellular matrix (ECM) can facilitate tumor cell mobility, promote immune evasion and stimulate tumor cell proliferation.[18,19] Conversely, ECM proteins such as collagen III can drive cancer cell dormancy, which slows tumor progression but also provides protection from anti-proliferative therapies.[20]

Despite recent insights into the complex role of fibrosis, predominantly in epithelial cancers, and the correlations between ECM gene expression and poor patient prognosis,[21] it remains unclear how CNS scarring may impact the response to therapy in glioblastoma. Here, we use an integrated multi-omics strategy to study fibrosis upon the treatment of glioblastoma and to identify targetable pathways to augment current treatments.

RESULTS

Regression of glioblastomas upon different treatment modalities is associated with fibrosis

To study fibrosis in the context of glioblastoma treatment, we first used the platelet-derived growth factor-driven glioma (PDG) transgenic mouse model (RCAS-hPDGF-B/Nestin-Tv-a; Ink4a/Arf$^{-/-}$, pure C57BL/6 background). Gliomas develop 4–5 weeks after tumor induction (Figure 1A) and closely model human proneural glioblastomas.[10,22–24] Similar to our earlier findings in a mixed genetic background PDG model,[10] we found that the response to the CSF-1R inhibitor BLZ945 consists of four key phases as measured by magnetic resonance imaging (MRI): regressing tumors (0–14-day post-treatment), dormant tumors (28-day), recurrent tumors (various time points), and dormant-until-endpoint tumors (Figure S1A). Immunofluorescence (IF) imaging and analysis of dormant residual lesions 28-days following BLZ945 treatment identified the presence of ECM-associated collagen type I throughout the lesion area (Figure 1B), in addition to aminopeptidase N (CD13) (Figure S1B), collagen IV, and fibronectin (Figure S1C). Further characterization revealed a compartmentalized structure consisting of a fibrotic core surrounded by reactive astrocytes, which were positive for glial fibrillary acidic protein (GFAP) (Figure S1B). Notably, this is similar to the organization of mature scars reported in non-tumor CNS pathologies, including traumatic brain injury, experimental autoimmune encephalomyelitis, and ischemic stroke.[25–27] Moreover, IF staining of recurrent gliomas, which were genetically labeled using green fluorescent protein (GFP), demonstrated the emergence of GFP^{+} tumor cells precisely from these regions of scarring (Figure S1C).

We found that mature BLZ945 treatment-associated scars could also be detected by T2-weighted MRI *in vivo*, where they are characterized by low signal intensity (Figure S1C, left panel). Subsequent correlative IF staining on the same tissue samples revealed that this low T2 MRI signal intensity corresponds to regions enriched in the expression of markers of CNS fibrosis (Figure S1C, right panels). Notably, recurrent tumors were always located directly next to these low T2 MRI signal intensity areas (n = 41) (Figure S1D), an observation that aligns with our finding that all recurrent tumors are found adjacent to histological scars.

We next investigated the prevalence of treatment-associated fibrosis across other glioma models and treatment modalities related to SoC therapy (Figures 1C–1F and S1E–S1H). To model the effect of ionizing radiation therapy (IR), mice bearing high-grade PDG were treated with focalized IR, and lesions were

(C) Schematic of preclinical trial for PDG tumors treated with 10 Gy whole-brain IR therapy.
(D and E) Representative IF image of 14-day post-IR PDG tumor (D) and HRas-GFAP-Cre tumor (E). Tumor cells labeled with GFP, astrocytes with GFAP, and fibrosis with Col I, Col IV, TNC, and fibronectin. Scale bars: 1 mm.
(F) Representative IF image of PDG tumor 14 days post-surgical resection. White arrow indicates resection cavity, green arrow indicates new tumor growth. Scale bar: 500 μm.
(G) Representative images of matched primary and recurrent glioblastoma patient samples, fibrosis labeled with Picrosirius red (PSR). Scale bars: 2 mm.
(H) Pathological scoring of fibrosis for primary and recurrent glioblastoma patient samples. Two-tailed t test p = 0.0023. Boxplots show median, upper and lower quartile, whiskers show upper and lower extreme, datapoints and outliers shown as dots.
(I) Representative IF images of recurrent high-grade GBM patient samples. Tumor cells labeled with Olig2, fibrosis labeled with Col I and TNC. Scale bars: 200 μm.
(J) Pre-operative MRI scans for glioblastoma patients with recurrent disease (I–III, top panel). White arrows indicate resection cavity from the initial surgery of the primary lesion, red boxes indicate sites of sample acquisition. IF images for each recurrent sample (I–III) are shown below. Asterisks indicate the location of prior resection cavity. Tumor cells labeled with Olig2/Sox2, fibrosis labeled with Col I, TNC, and PDGFRB. Scale bars: 200 μm.
See also Figure S1.

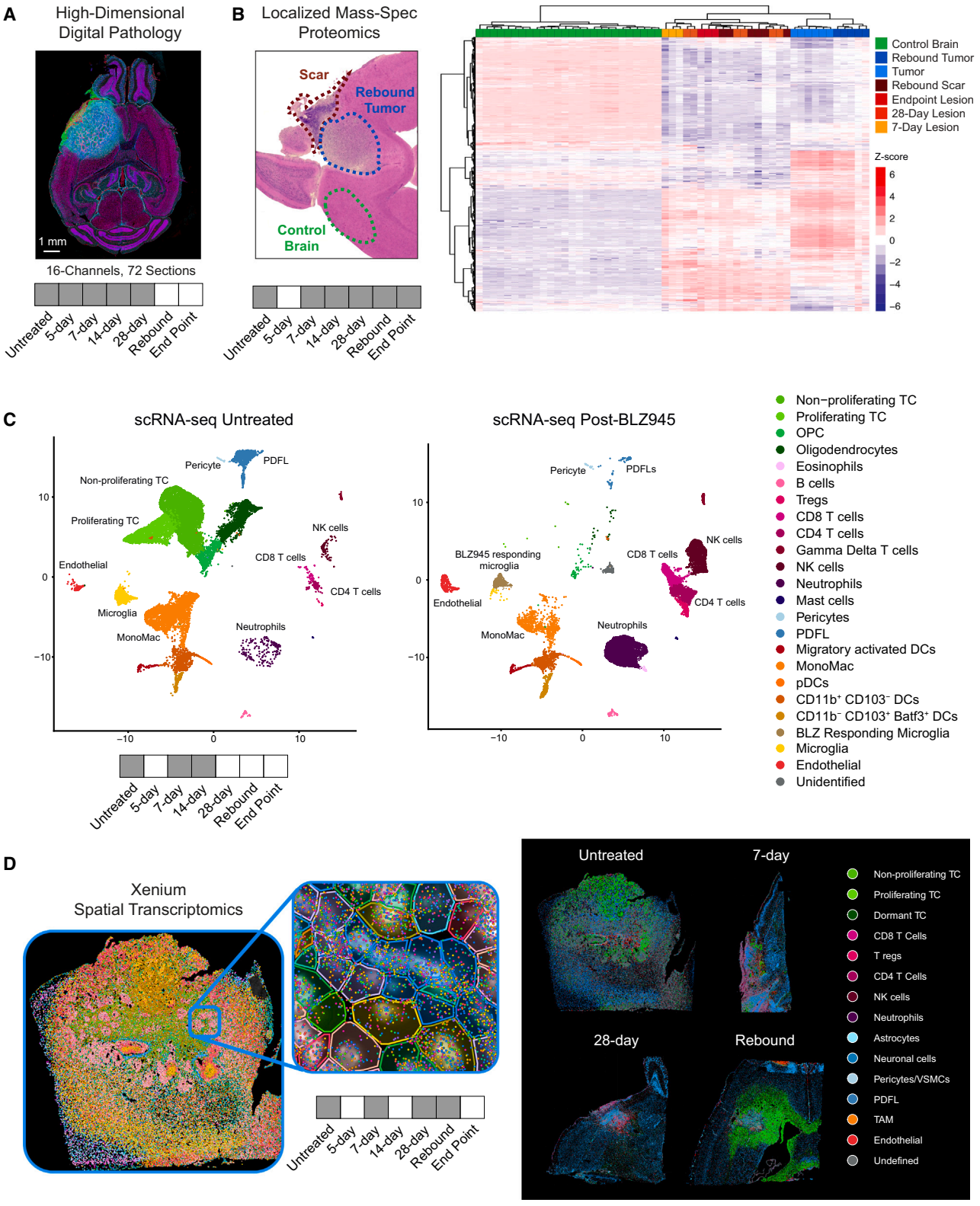

Figure 2. Integrated spatial multi-omics characterizes the post-treatment glioma microenvironment

(A) Representative image of untreated PDG tissue section analyzed by hyperplexed immunofluorescence imaging (HIFI)-based digital pathology. Gray boxes below indicate BLZ945 treatment time points assessed, white boxes are time points not assessed. *N* = 3 mice per time point, *n* = 4 images per mouse.

(legend continued on next page)

analyzed 7 days post-treatment (Figure 1C). Mice treated with IR showed similar low T2 MRI signals in association with the treated lesions (Figure S1E, left panel) as observed following BLZ945 treatment, and increased abundance of collagen I (which represents a readout for fibrosis) and TNC by IF analysis (Figure 1D). In longer-term IR trials, tumor recurrence occurred immediately adjacent to these structures (Figure S1E, right panel) as we had found for BLZ945 treatment (Figure S1D). This IR experiment was repeated in two distinctive glioma models: HRas-GFAP-Cre and GL261. The HRas-GFAP-Cre model involves activation of the HRasV12 oncogene combined with p53 knockdown in GFAP-expressing cells.[28,29] Importantly, this tumor model develops in the mouse hippocampus, different from the prefrontal cortex location of PDG gliomas, and mice have a different genetic background (FVB/n, vs. C57Bl/6J for PDG and GL261). Both HRas-GFAP-Cre and GL261 tumors showed similar fibrosis marker expression at 7- and 14-days post-IR (Figures 1E, S1G, and S1H). We also performed partial surgical resection on established PDG tumors (Figure 1F). IF analysis of 14-days post-resection samples revealed patterns of fibrosis immediately adjacent to the original resection cavity (Figure 1F), again comparable to post-BLZ945 treatment. In addition, there was an evident correlation between new tumor growth and fibrosis associated with the resection cavity (Figures 1F and S1F). There was no observed dormancy phase for this treatment modality, as surgical resections resulted in incomplete removal of the tumor mass by design.

Evidence for treatment-induced fibrosis in glioblastoma patients

To determine whether these preclinical findings correlated with the SoC treatment response in patients, we collected matched primary and recurrent glioblastoma patient samples that were analyzed by hematoxylin and eosin (H&E), as well as by Picrosirius red (PSR) staining to visualize collagen, representing a surrogate of fibrosis (Figure 1G). Pathological assessment of H&E and PSR images showed that recurrent samples exhibited significantly increased fibrosis compared to primary tumor samples (Figures 1H and S1I). Moreover, IF staining of recurrent patient tumors demonstrated the spatial architecture of ECM proteins and associated neoplastic cells (Figure 1I), similar to our findings following the different treatments performed in murine models. Together with neurosurgeons and radiologists, we also performed MRI-guided selection of suspected fibrotic regions (Figure 1J, top panels), found near the resection cavity of the original primary lesion, before the surgery of recurrent high-grade glioblastomas. Again, in this optimally controlled context, IF imaging identified fibrotic responses immediately adjacent to the resection cavity (Figure 1J, bottom panels), similar to our findings in mouse models of surgical resection (Figure 1F).

Integrated multi-omics analysis of treatment-associated glioma fibrosis

To comprehensively interrogate the complex cellular and extracellular composition of treatment-associated fibrosis we employed an integrated multi-omics analysis strategy. We decided to analyze the microenvironmental response to CSF-1R inhibition using BLZ945, given its marked effect on tumor regression and increased survival in mouse models, notably as compared to standard-of-care therapies.[10,12] Moreover, a phase I/II trial in patients combining BLZ945 with the anti-PD-1 monoclonal antibody spartalizumab reported interim results showing antitumor efficacy in some patients (https://doi.org/10.1158/1538-7445.AM2020-CT171).

Hyperplexed immunofluorescence imaging (HIFI) whole-slide digital pathology[30] was used to spatially localize cellular phenotypes and the structural organization of sub-regions across a range of post-treatment time points (Figures 2A and S2A; Table S1). We additionally performed unbiased mass spectrometry (MS)-based proteomic analysis of different tissue areas (tumor, contralateral healthy brain, and fibrotic scar areas) isolated from BLZ945-treated PDGs at multiple post-treatment time points (Figure 2B). Analysis of the proteomic composition of pre- and post-treatment tumor domains revealed several key insights. First, we observed that all healthy brain samples clustered closely together across treatment time points (Figure 2B, right panel). Next, we found that untreated and rebound tumor samples clustered independently, demonstrating clear compositional changes at the point of recurrence (Figure 2B). Finally, all post-treatment lesion samples clustered together with fibrotic scars isolated from rebound tumor samples, indicating that all lesions had similar fibrotic profiles following treatment, even as early as 7 days post-treatment (Figure 2B).

To further evaluate the cellular phenotypes in untreated and BLZ945-treated glioblastomas, we performed single-cell RNA-sequencing (scRNA-seq) on untreated, and 7- and 14-day-treated PDG tumors (Figures 2C and S2B). Samples were dissociated using a specific digestion protocol to preserve rare surviving tumor cells and vascular-associated cells.[31,32] Following BLZ945, several cell populations were increased, including neutrophils, natural killer (NK) cells, various dendritic cell (DC) subtypes, $CD8^+$ T cells, $CD4^+$ T cells, gamma-delta ($\gamma\delta$) T cells, and regulatory T cells (Tregs), while tumor cells were almost completely absent (Figures 2C and S2C). While measures were taken to preserve cell viability following dissociation, differential loss of cellular populations due to tissue digestion could not be ruled out. Indeed, when comparing cell abundance analysis between scRNA-seq (Figure S2C) and HIFI data (Figure 3A), some cellular populations are underrepresented in the scRNA-seq data. This highlights the importance of orthogonal multi-omics analyses for accurate data interpretation.

(B) Representative H&E-stained tissue sections used to guide manual microdissection of tissue regions for mass spectrometry proteomic analysis (left panel). Hierarchical clustered heatmap of protein abundance *Z* scores from tissue regions collected at each treatment time point (right panel).
(C) UMAP projection of scRNA-seq analysis of untreated tumors (left, $n = 3$), and combined 7- and 14-day BLZ945-treated tumors (right, $n = 6$). TC = tumor cell.
(D) Representative image of Xenium-based single-cell spatial transcriptomics (ST) of untreated PDG tissue section with unbiased cell clustering colored for clarity (left). Insert shows high-magnification image with cell outlines and individual mRNA transcripts detected as dots. Right panel shows representative images of pre- and post-BLZ945 treated PDG tumors with annotated cell types colored accordingly. $n = 3$ for each time point.
See also Figure S2 and Tables S1, S2, S3, and S4.

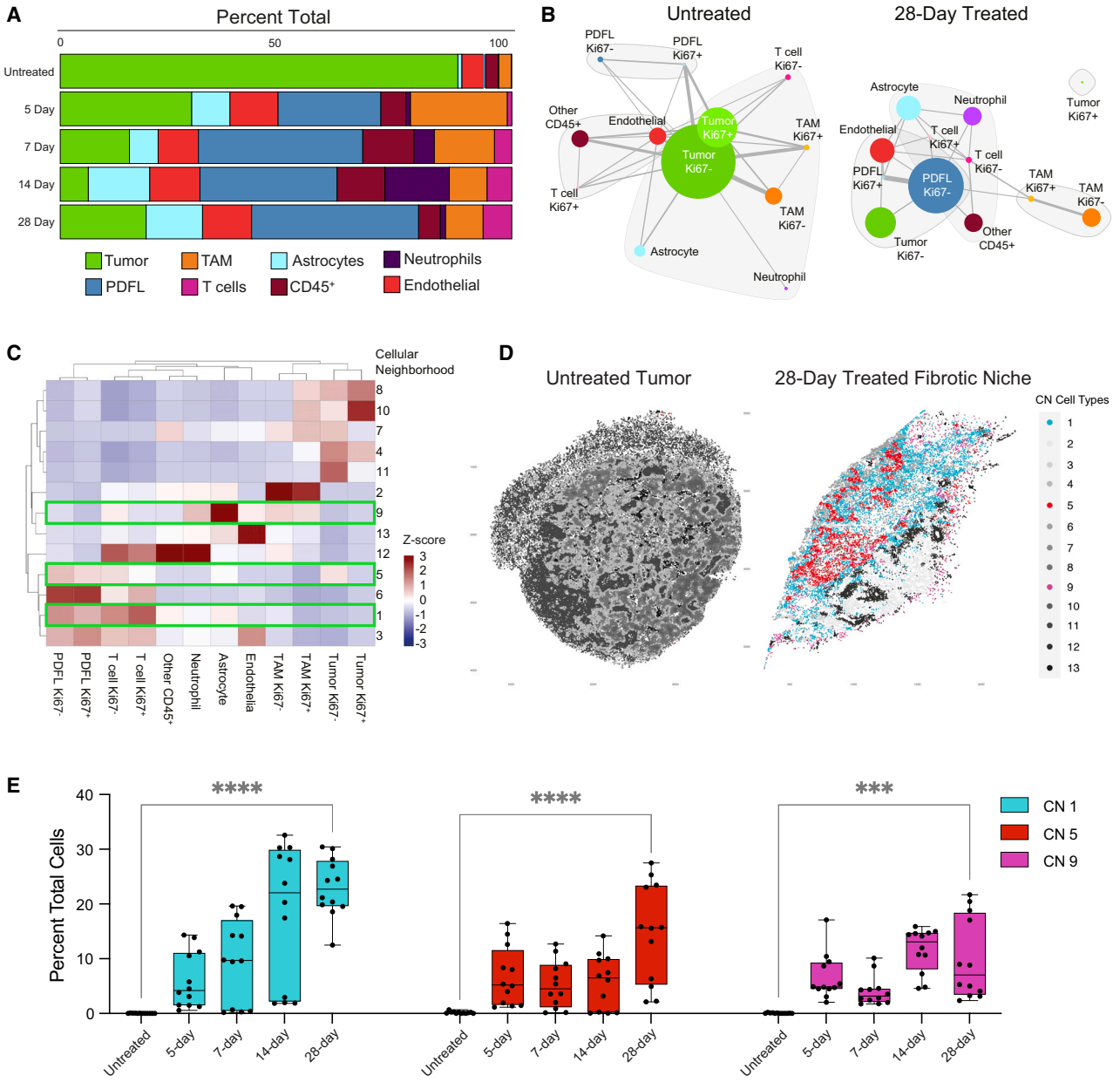

Figure 3. Digital pathology spatial analysis of post-treatment cellular architecture

(A) Stacked bar plots of percent-total cell populations derived from image analysis of indicated treatment time points.

(B) Graph network analysis plots of pooled untreated and 28-day BLZ945 treated samples. Node sizes represent ranges of percent-total for each cell type, from >50% to <1%. Edge length is the mean distance between nearest neighbors of each cell type using the Fruchterman-Reingold layout. Edge thickness represents constancy for cellular colocalization (1/standard deviation of mean).

(C) Hierarchal clustered heatmap of relative abundance *Z* scores for each cell-type in each identified cell neighborhood (CN), 1–13. Green boxes indicate CNs of interest.

(D) Representative spatial distribution plots for selected CNs in untreated (left) and 28-day BLZ945-treated (right) samples.

(E) Percent-total of cells belonging to cell neighborhoods (CN) 1, 5, and 9 at each BLZ945 treatment time point. Two-way ANOVA, ****$p < 0.0001$, ***$p = 0.0007$. Boxplots show median, upper and lower quartile, whiskers show upper and lower extreme, datapoints and outliers shown as dots. See also Figure S3.

To validate gene expression as an *in situ* "ground truth"[33,34] and to provide critical spatial context for scRNA-seq data, we performed single-cell resolution *in situ* sequencing-based spatial transcriptomics (ST) using the Xenium platform (10× Genomics) (Figure 2D). Untreated, 7-day, 28-day, and rebound PDG tumor samples were analyzed with a panel of 247 murine brain-tumor specific genes that was supplemented with 100 additional genes informed by our scRNA-seq data (Table S2). HIFI was performed on slides following Xenium analysis to provide critical intra- and extracellular protein localization data (Table S3).

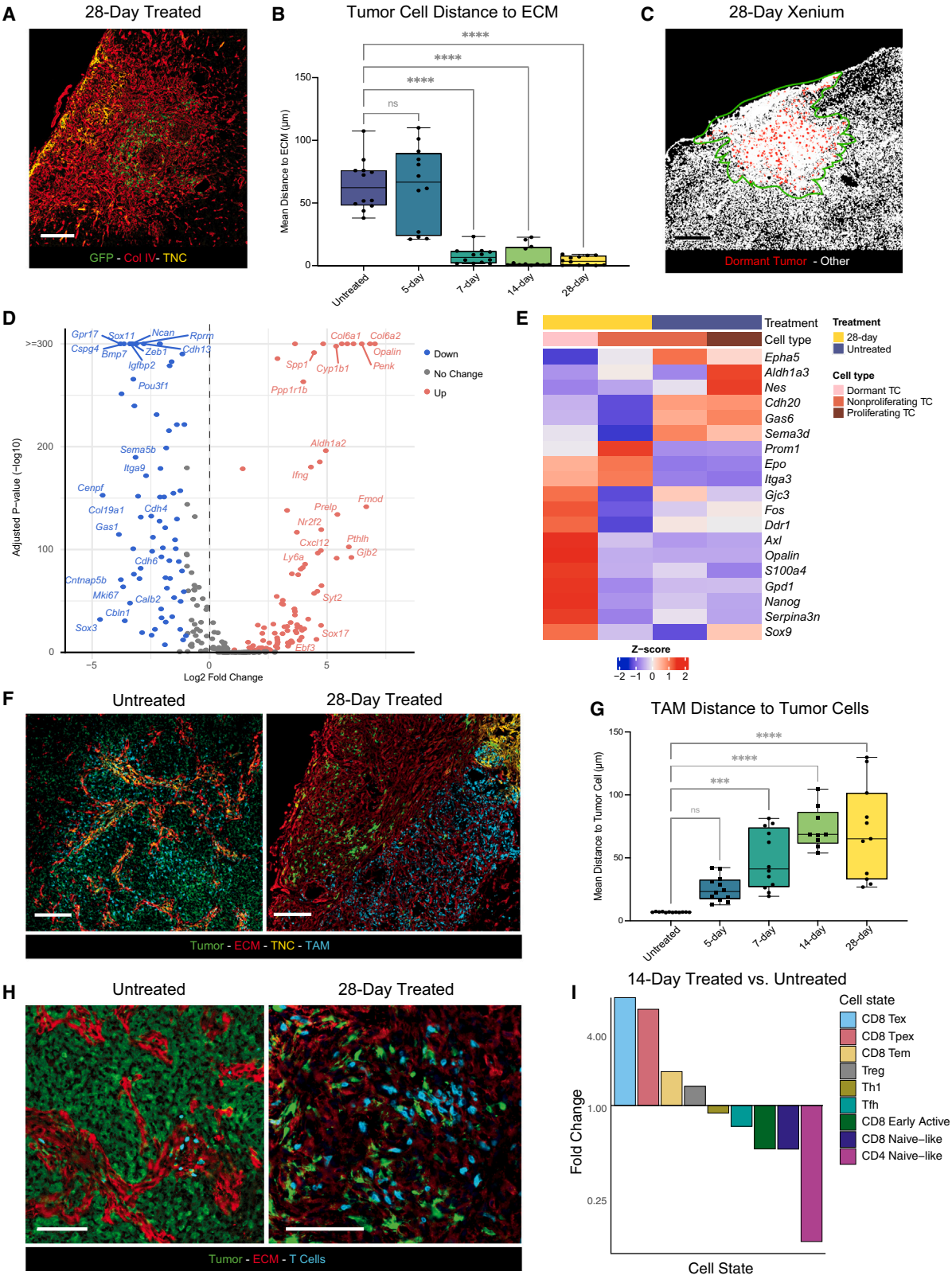

(legend on next page)

Machine-learning annotation for regions of fibrosis was performed on HIFI data and integrated into ST data to measure single-cell proximity to areas of fibrosis. Unsupervised cluster analysis was performed on single-cell ST data, and a combination of semi-supervised gene signatures and cell type projection from scRNA-seq data was used for cell classification (Figures 2D; Table S4).

CNS fibrosis as a protective niche for dormant tumor cells following BLZ945 treatment

Analysis of HIFI data revealed that fibrotic ECM-positive areas gradually increase as the percentage of total lesion area following tumor regression in response to CSF-1R inhibition, reaching a maximum at 28 days of treatment (Figure S3A). This coincided with an increased prevalence of CNS scar-associated cell types including perivascular-derived fibroblast-like cells (PDFLs) and astrocytes, as well as immune cell types such as TAMs, T cells, and neutrophils (Figure 3A). In untreated tumors and in normal brain tissue, PDFLs (ER-TR7$^+$) were detected in association with the vasculature within the parenchyma (Figure S3B). Notably, in previous studies investigating distinct insults to brain tissue, PDFLs were shown to delaminate from the CNS vasculature, differentiate, and proliferate to produce ECM proteins.[27,35,36]

Next, we employed orthogonal graph-based network analysis to analyze the spatial relationships of specific cell types in HIFI data from untreated and post-BLZ945-treated PDG lesions[30] (Figures 3B and S3C). A comparison of network plots between untreated tumors versus 28 days of BLZ945 revealed that surviving tumor cells and T cells become closely associated with PDFLs (Figure 3B). By contrast, in dormant lesions, TAMs are largely excluded from regions containing tumor cells (Figure 3B). We used cluster-based cell neighborhood analysis to further explore cellular spatial relationships and classify cells based on the cellular proportions of their immediate environment across different treatment time points.[37] Hierarchical clustering revealed 13 different cellular neighborhoods (CN) in the pooled data from all treatment conditions (Figure 3C). We quantified the CNs across time points to investigate how these neighborhoods changed in response to BLZ945 treatment (Figure S3D). CN1, CN5, and CN9 increased throughout treatment and were largely absent in untreated samples (Figure 3D left panel, and 3E). CN5 and CN1, containing PDFLs and T cells with or without tumor cells, respectively (Figure 3C), colocalize in treated lesions, whereas CN9, containing TAMs, astrocytes, and neutrophils, is spatially excluded from CN5 and CN1 (Figure 3D, right panel).

We visually validated and additionally quantified cellular localization from the HIFI data to corroborate the results from the network and neighborhood spatial analyses (Figures 4A, 4F, 4H, and S4A–S4C). We indeed observed a significant increase in association between surviving tumor cells and domains of dense ECM accumulation as defined by machine learning annotation (Figures 4A and 4B) and high TNC expression (Figure S4A) in images of lesions treated with BLZ945. This exact, consistent localization was observable at 16 weeks post-treatment (Figure S4C), demonstrating that glioblastoma cells can persist within fibrotic regions for many months after treatment. Conversely, ECM domains and associated PDFL cells were predominantly countercorrelated with tumor cells prior to treatment (Figures 3B and S4B).

Our HIFI analysis showed that tumor cells associated with post-treatment fibrosis were non-proliferative (Figure 3B), suggesting that tumor cells in this niche were in a dormant or quiescent state. To further investigate the phenotype of surviving tumor cells, we analyzed Xenium ST data of tumor cells within 28-day post-treatment fibrotic scars and compared differentially expressed genes (DEGs) to untreated tumor cells (Figures 4C–4E, S4D, and S4E; Table S5). As expected, we observed a multi-fold reduction in proliferation-related genes such as *Mki67* and *Cenpf* in post-treatment tumor cells compared to untreated (Figures 4D and S4D). Notably, cluster analysis revealed two distinct subclusters of tumor cells in 28-day scars: non-proliferating tumor cells and dormant tumor cells with significantly enhanced expression of multiple dormancy and stemness-related genes (Figures 4E and S4E). In particular, *Gpd1*, *Nanog*, and *Sox9* expression were all significantly and uniquely associated with dormant post-treatment tumor cells and have

Figure 4. Pro-survival features of the post-treatment fibrotic niche

(A) Representative IF image of PDG lesion following 28-day of BLZ945 treatment. Tumor cells labeled with GFP, fibrosis labeled with Col IV. Scale bar: 200 μm.

(B) Mean distance of tumor cells in HIFI data to the nearest fibrotic ECM region annotations for each treatment time point. Two-way ANOVA ****$p < 0.0001$, ns = non-significant. Boxplots show median, upper and lower quartile, whiskers show upper and lower extreme, datapoints and outliers shown as dots.

(C) Representative Xenium ST image and distribution plot of 28-day BLZ945 treated PDG lesion, dormant tumor cells (red) labeled in region of fibrosis (green border). Scale bar: 200 μm.

(D) Volcano plot of differentially expressed genes (DEGs) in Xenium ST data for tumor cells in untreated samples ($n = 3$) vs. fibrosis-embedded tumor cells in 28-day samples ($n = 3$). DEGs with p value <0.05 and log2 fold change >1 labeled as increased (red) or decreased (blue) in 28-day BLZ945-treated tumor cells compared to untreated controls.

(E) Heatmap of Z scores for selected dormancy and stemness-related DEGs in ST analysis of tumor cells (TC) annotated as dormant, non-proliferating, and proliferating in untreated ($n = 3$) and 28-day BLZ945-treated ($n = 3$) PDG lesions.

(F) Representative IF images of untreated (left) and 28-day BLZ945-treated (right) samples. Tumor cells labeled with GFP, tumor associated macrophages (TAMs) with CD68, and ECM with collagen I. Scale bars: 200 μm.

(G) Mean distance of "TAM" cells in HIFI data to nearest "tumor cell" neighbor in each image ($n = 12$) for each treatment time point. Two-way ANOVA ****$p < 0.0001$, ***$p = 0.0002$.

(H) Representative IF images of untreated (left) and 28-day BLZ945-treated (right) samples. Tumor cells labeled with GFP, T cells with CD3, and ECM with collagen I. Scale bars: 200 μm.

(I) Rank-ordered bar plot of fold-changes in T cell phenotypes from 14-day BLZ945-treated tumors versus untreated tumors. ProjectTILs analysis of scRNA-seq data identified CD8$^+$ terminally exhausted (CD8$^+$ Tex), CD8$^+$ precursor-exhausted (CD8$^+$ Pex), CD8$^+$ T effector-memory cells (CD8$^+$ Tem), regulatory T cells (Treg), type 1 T helper (Th1), CD4$^+$ T-follicular helper cells (Tfh), CD8$^+$ early active, CD8$^+$ naive-like, and CD4$^+$ naive-like T cell phenotypes.

See also Figures S4 and S5, and Table S5.

each been previously associated with dormancy and the concept of "glioma stem cells" (GSCs).[38–40] Taken together, these data indicate that surviving tumor cells in fibrotic spatial niches reside in a dormant stem-like state. Previous studies have demonstrated how similar cell states in patients are associated with resistance to treatments targeting cancer cells, including IR and chemotherapy.[41,42]

Tumor cells embedded within fibrotic regions were also found to be spatially separated from BLZ945-re-educated TAMs (Figure 4F). Over the course of early BLZ945 treatment, the distance between TAMs and tumor cells progressively increases until day 28 post-treatment (Figure 4G). In our HIFI data, we could not definitively discriminate between resident microglia and infiltrating macrophages. In studies of other non-tumor CNS pathologies, analyses of mature scars that develop within weeks after the initial stimulus[43] reported that activated microglia are close to the astrocytic border surrounding the fibrotic core.[44] Given that our analyses show the core contains surviving tumor cells, these results suggest that treatment-induced fibrosis may physically protect glioma cells from anti-tumor immunity. However, we additionally observed a progressive increase in the percentage of T cells in treated glioblastomas (Figure 3B), which are found in association with the surviving tumor cells (Figures 4H and 3C). To query the functionality and potential heterogeneity of these T cells, we used the nearest-neighbor classifier of the ProjecTILs algorithm[45] to predict T cell states within the scRNA-seq dataset (Figure S5A). Applying this algorithm to the single-cell data from BLZ945-treated tumors revealed a progressive increase in exhausted, non-functional T cell phenotypes and in regulatory T cells (Figures 4I and S5A). Moreover, applying T cell exhaustion scores to single-cell ST data for $CD4^+$ and $CD8^+$ T cells, and Treg populations revealed that T cell exhaustion was significantly enhanced in regions of fibrosis compared to T cells outside of fibrosis (Figure S5B).

These findings suggest that domains of treatment-associated fibrosis can act as protective niches for surviving tumor cells, promoting dormant stem-like treatment-resistant phenotypes, and further protecting them from macrophage and T cell-mediated immune surveillance. In both IR and surgical resection treatment models, we observed similar embedding of surviving tumor cells in TNC-high ECM, increases in T cells associated with fibrosis, and exclusion of CD68-high macrophages from ECM-embedded tumor nests (Figure S5C). This suggests that any treatment that aggressively perturbs the TME has the potential to trigger a fibrotic response with characteristics similar to what we observe following BLZ945 treatment of PDG tumors.

Treatment-associated fibrosis potentiates glioblastoma recurrence

HIFI analysis of the interface between post-treatment fibrotic regions and rebound PDG tumors revealed a complex interplay between tumor cells embedded in fibrosis and those regrowing in the brain parenchyma (Figures 5A and S5D). Differential protein analysis of spatially resolved proteomic data showed that fibrotic regions had significantly higher expression of multiple mitogenic and growth-promoting ligands compared to adjacent rebound tumors and contralateral healthy brain (Figure 5B).

Xenium ST analysis of rebound tumor samples provided additional evidence that the fibrotic niche was the cellular source of rebound tumor cells. Rebound tumor samples in the ST dataset were binned into four compartments based on their relative distance to the post-treatment fibrotic niche (Figure 5C). Analysis of DEGs was performed by comparing each zone of proliferating rebound cells to proliferating untreated tumor cells, and 28-day post-treatment dormant tumor cells within fibrosis (Figure S5E). Proliferating rebound tumor cells uniquely clustered independently from both dormant tumor cells and untreated proliferating tumor cells, evidencing marked disparity to pretreatment phenotypes. Notably, a cluster of DEGs revealed transcriptional similarity between dormant tumor cells and rebound tumor cells (Figures 5D and S5E). Dormant tumor cells clustered primarily with rebound zones 1 and 2 closest to fibrosis, followed by zones 3 and 4, all of which were distinct from untreated tumor cells (Figure 5D).

Taken together with our other orthogonal data, this suggests that the fibrotic niche supports survival of dormant stem-like tumor cells, and that rebound growth is driven by tumor cell escape from fibrotic structures into a growth- and migration-stimulating local environment.

CNS fibrosis is associated with increased TGF-β and inflammatory signaling in PDFLs

Investigation of the proteins significantly enhanced in fibrotic scars identified a range of ECM and ECM-remodeling proteins in proteomic data including collagens, fibrillins, DCN, MMP19, and SPP1 (Figure 6A). We interrogated the expression of genes encoding these scar-related factors in scRNA-seq data for multiple cell phenotypes that were found to localize to fibrotic regions in ST data at 7- and 14-days post-treatment (Figure 6B). We observed that PDFL cells had the highest relative gene expression for scar-related factors, except for *Mmp19* and *Tgfbi* that were highest in the monocyte/macrophage population (Figure 6B).

Gene set enrichment analyses (GSEA) of proteomic data, comparing fibrotic scars to both tumor and healthy brain samples (Figures 6C and S6A), revealed significant enrichment of multiple pathways in fibrosis relating to inflammation, wound healing, transforming growth factor β (TGF-β) signaling, and ECM remodeling. When we examined the proteins most highly represented in the leading edge of enriched gene sets, we identified several prominent factors, including TGF-β1, WNT5A, COL3A1, COL1A1, and DCN (Figure S6B). Next, we queried the scRNA-seq data for cellular populations with high expression of these leading-edge genes. We identified a subset of PDFLs that showed high expression of scar-related proteins, which were primarily associated with post-treatment samples (Figure 6D). This PDFL population tended to cluster with vascular pericytes in dimensional reduction (Figures 2C and 6D) and was localized to regions of post-treatment fibrosis in ST data (Figure S6C). The larger pre-treatment pericyte phenotype cluster was depleted following treatment, which suggests either a selection for PDFLs over pericytes, or a possible differentiation of pericytes toward the PDFL phenotype.

Next, we applied the NicheNet method to model potential intercellular communication by linking upregulated genes to alterations in respective ligand-receptor expression.[46] We integrated spatial colocalization data derived from HIFI analysis with NicheNet to weigh and filter cell communication interactions

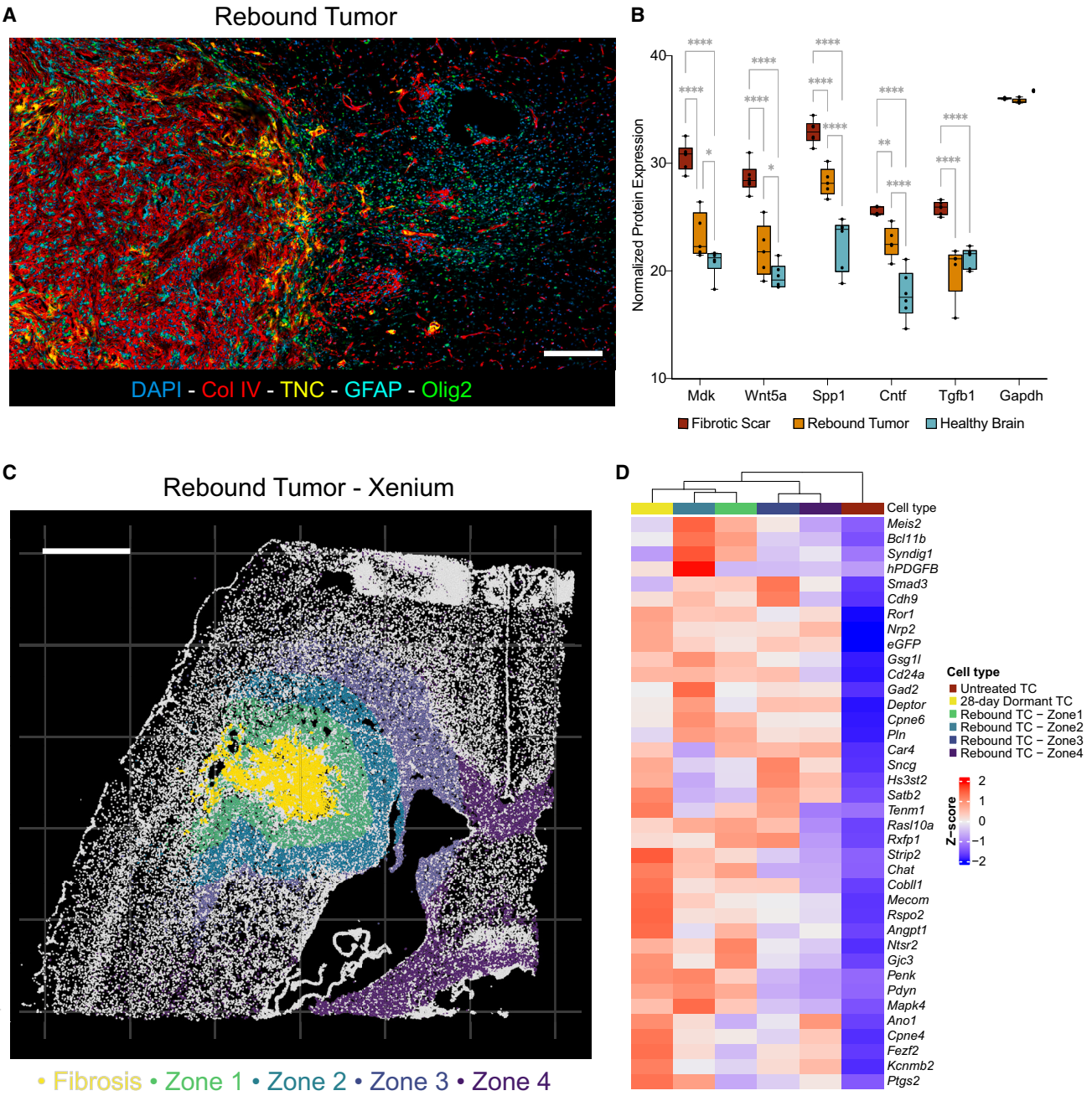

Figure 5. Pro-recurrence features of the post-treatment fibrotic niche

(A) Representative IF image of interface between post-BLZ945 treatment-associated fibrosis and early rebound tumor. Tumor cells labeled with Olig2, fibrosis labeled with Col IV and TNC, and astrocytes labeled with GFAP. Scale bar: 100 μm.

(B) Normalized protein expression of growth factors and GAPDH control from mass-spec proteomic analysis of BLZ945-treated fibrotic scars ($n = 5$), immediately adjacent rebound tumors ($n = 5$), and contralateral healthy brain ($n = 5$). Two-way ANOVA ****$p < 0.0001$, *$p = 0.0197$, *$p = 0.0221$, **$p = 0.0062$. Boxplots show median, upper and lower quartile, whiskers show upper and lower extreme, datapoints and outliers shown as dots.

(C) Representative Xenium ST distribution plot of proliferating rebound tumor cells subdivided into 4 concentric zones based on distance from treatment-associated fibrotic niche. Scale bar: 500 μm.

(D) Heatmap of DEG *Z* scores for "cluster 2" DEGs (Figure S5E) in ST analysis of proliferating tumor cells in untreated samples ($n = 3$), and zones 1–4 of rebound samples ($n = 3$) vs. dormant tumor cells in 28-day treated samples ($n = 3$).

See also Figure S5.

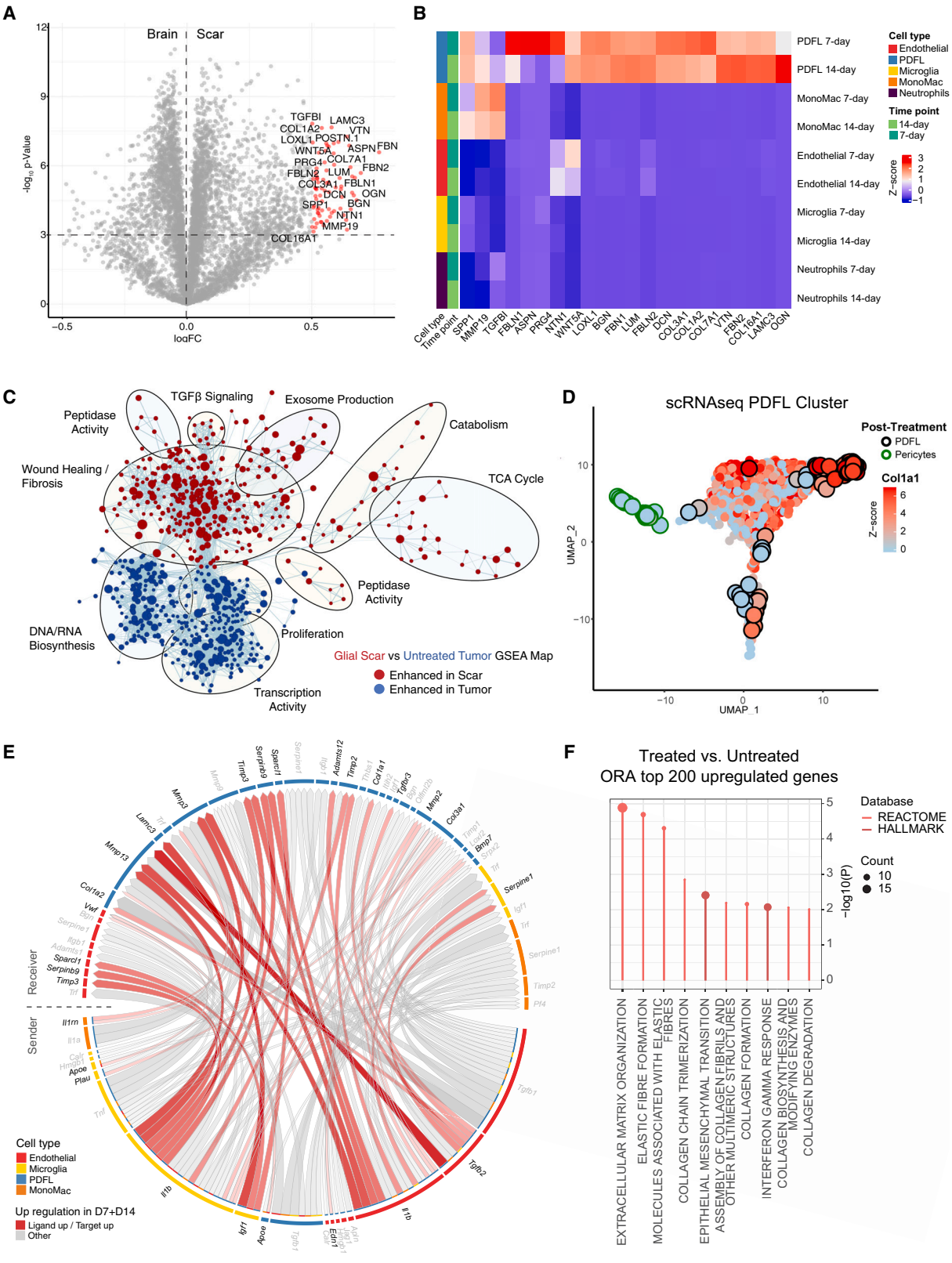

(legend on next page)

based on the probability of cellular association *in vivo*. We found that many different cell types in BLZ945-treated tumors contribute to networks of interactions that enhance pathways identified in the analysis of the proteomics dataset (Figures 6E and S6D). Cell populations corresponding to PDFLs appeared to be the main biosensor of the environment, with many signals from multiple cell types driving downstream target gene alterations (Figures 6E and S6D). Of specific interest were enhanced expression of *Col1a1*, *Col1a2*, *Col3a1*, and *Mmp3* in PDFLs being linked to TGF-β signaling (via *Tgfb1* and *Tgfb2*), and proinflammatory cytokine genes *Tnf*, *Il1a*, and *Il1b* from macrophages, microglia, and endothelial cells. Analysis of matched HIFI and ST data showed that PDFLs specifically in the fibrotic regions of 7-day post-treatment samples demonstrated the highest co-expression of *Col1a1* and *Tgfbr2* (Figure S6E). This indicates that PDFLs shortly after treatment had uniquely high expression of both the key component of the TGF-β receptor dimer, and a core constituent of fibrotic ECM. We therefore explored the most significant gene expression changes in PDFLs upon BLZ945 treatment (Table S6). Upregulated genes included collagen IV (*Col4a5* and *Col4a3bp*), the chemokine *Cxcl12,* and the adhesion molecule *Vcam1*. Subsequent overrepresentation analysis (ORA) of genes upregulated in PDFLs in treated versus untreated glioblastomas revealed a multifaceted response incorporating Epithelial-Mesenchymal Transition (EMT), indicative of fibroblast differentiation through EMT,[47] interferon gamma response (IFN), and multiple pathways related to ECM formation and organization (Figure 6F).

Together, these results suggest that PDFL cells are a major contributor to treatment-induced scarring via the production of ECM and recruitment of immune cells in response to TGF-β and inflammatory signaling.

PDFL cells in TME show rapid and acute response to BLZ945

The profound fibrotic response observed after just 7 days of BLZ945 led us to investigate the temporal dynamics of fibrosis and PDFLs following treatment. Indeed, IF to visualize ER-TR7$^+$ PDFLs revealed a rapid cellular response to treatment initiation with a significant expansion of PDFLs within the first 3 days following treatment initiation, resulting in complete lesion coverage by day 5 (Figure S7A).

Using integrated single-cell RNA-seq and spatial transcriptomic data, we employed NicheNet analysis to interrogate the cellular communication of PDFLs specifically within fibrotic scars at 7 days post-BLZ945 (Figure 7A). Based on our global cell communication analysis (Figure 6E), we focused on the TGF-β signaling pathway and sender populations with the highest level of TGF-β ligand expression; MonoMac, microglia, endothelial, and PDFLs (Figure 7A). Interestingly, only *Tgfb1* showed significantly increased regulatory potential at 7 days post-treatment, driving increased expression of the TGF-β receptor *Tgfbr2*, and multiple ECM and ECM-remodeling pathway genes including *Col1a2*, *Elastin*, and *Junb* (Figure 7A). This analysis further demonstrated extensive TGF-β signaling to PDFL cells, driving the expression of fibrotic scar-related genes, consistent with NicheNet analysis of disaggregated scRNA-seq data (Figure 6E).

Overrepresentation analysis comparing PDFL single-cell gene expression in 7-day-treated PDGs versus untreated PDGs showed significant increases in gene sets related to EMT, ECM organization, and interferon signaling (Figure 7B, top panel). These processes are consistent with perivascular cells undergoing EMT and differentiating into fibroblast-like cells that subsequently produce many of the same ECM proteins identified in our proteomic analysis (Figure 2B). This indicates a rapid response by this population following therapeutic perturbation.

When comparing PDFL gene expression at 14 days of treatment versus 7 days of treatment, several of these same gene sets were downregulated (Figure 7B, bottom panel), indicating a transient activation state of PDFLs following the initiation of treatment. Next, we generated four gene signatures (EMT, ECM, IFNγ, and IFNα) of PDFL treatment response based on the HALLMARK and REACTOME gene sets, which showed differential expression between the three treatment time points (Table S7). Comparison of gene signature expression at each time point revealed a rapid increase from untreated to 7 days of treatment, followed by either a plateau or a marked decrease in expression level at 14 days of treatment (Figure 7C). Together with the HIFI data, these results suggest that the potential window to inhibit treatment-associated fibrosis is immediately at the initiation of treatment, and up to ∼7–14 days thereafter. Following this short window, stable fibrotic structures appear established, and the targetable pathways resulting in their formation decrease spontaneously.

To investigate if similar early activation phenotypes were present in the patient setting, we compared the scRNA-seq expression profiles of 7- and 14-day post-treatment PDFLs to single-cell transcriptomic studies of fibroblast-like cells in human

Figure 6. Cellular communication underlying protein composition of fibrosis

(A) Volcano plot of differential protein abundance in mass-spec proteomic data of 28-day post-BLZ945 treated fibrotic scar samples (n = 5) vs. contralateral healthy brain controls (n = 5). Proteins with -log10 p-values >3 and log fold change >0.5 labeled as increased (red) in fibrotic scar samples.

(B) Heatmap of DEG Z scores from scRNA-seq analysis of DEGs corresponding to proteins identified in Figure 6A.

(C) GSEA enrichment mapping of significantly enhanced gene sets ($p < 0.001$) between fibrotic scars of rebound tumors versus untreated tumors. GSEA employed Hallmark, Biocarta, Reactome, KEGG, and GO databases.

(D) UMAP projection of perivascular-derived fibroblast-like cells (PDFLs) and pericyte clusters from scRNA-seq analysis of untreated (n = 3), 7-day BLZ945 treated (n = 3) and 14-day treated (n = 3) tumors. Blue-to-red gradient shows scaled *Col1a1* expression. Black and green borders indicate cells from post-treatment samples.

(E) Circos plot of HIFI-weighted NicheNet cellular communication analysis of untreated and pooled 7- and 14-day-BLZ945 treated tumors derived from scRNA-seq analysis. Green arrows indicate interactions where both ligand and target gene show increased expression in post-BLZ945 treated samples (n = 6) compared to untreated (n = 3).

(F) Overrepresentation analysis (ORA) of top 200 genes upregulated in PDFLs from BLZ945-treated tumors (n = 6) versus untreated tumors (n = 3). GSEA employed Hallmark and Reactome databases.

See also Figure S6 and Table S6.

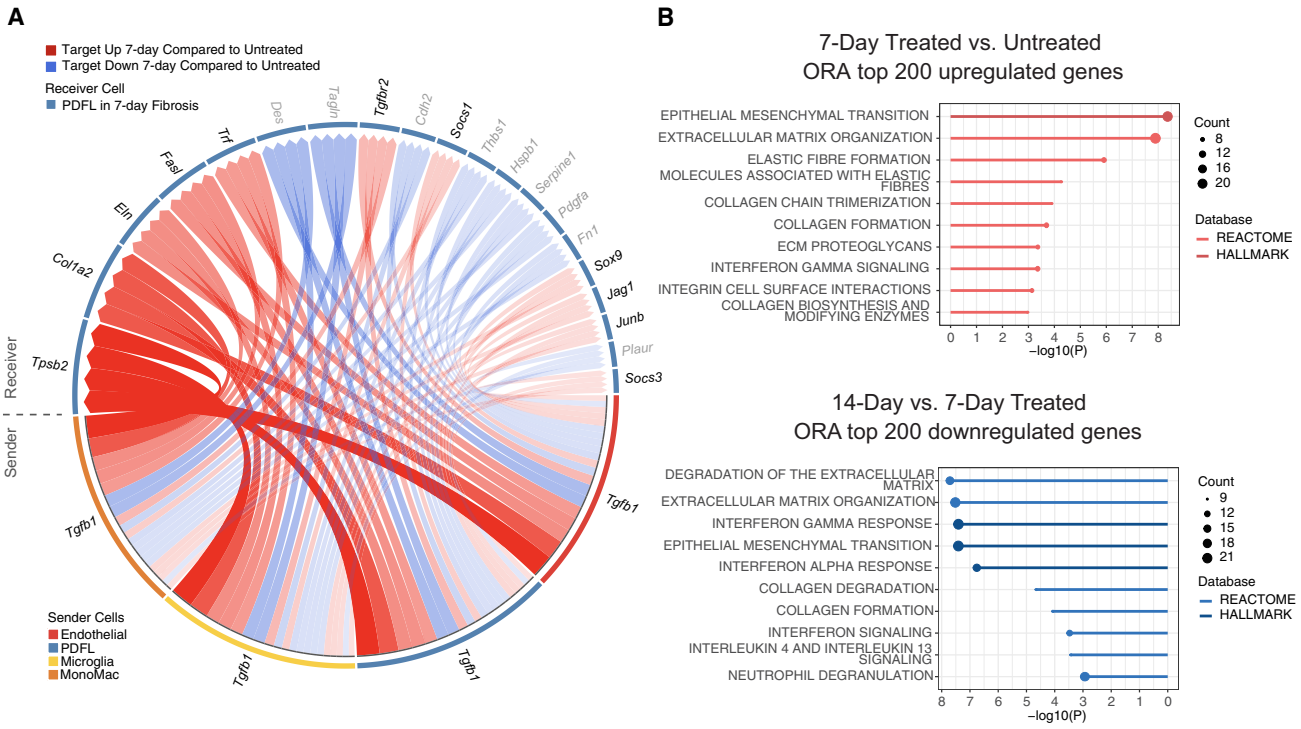

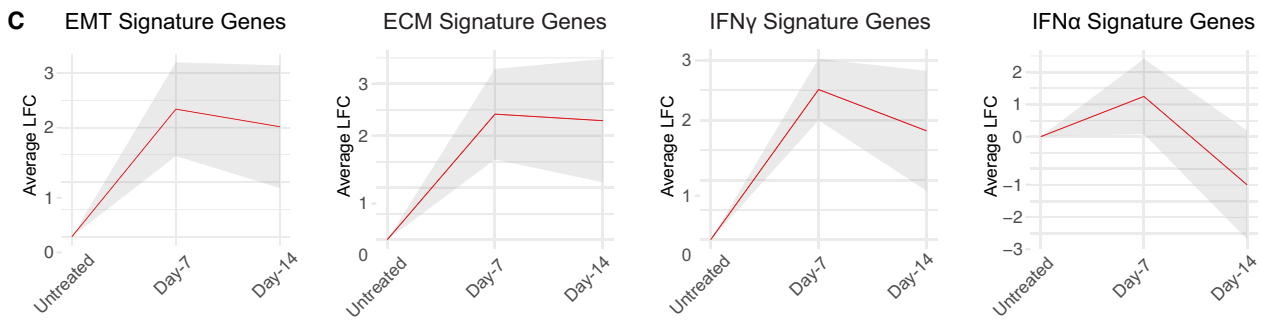

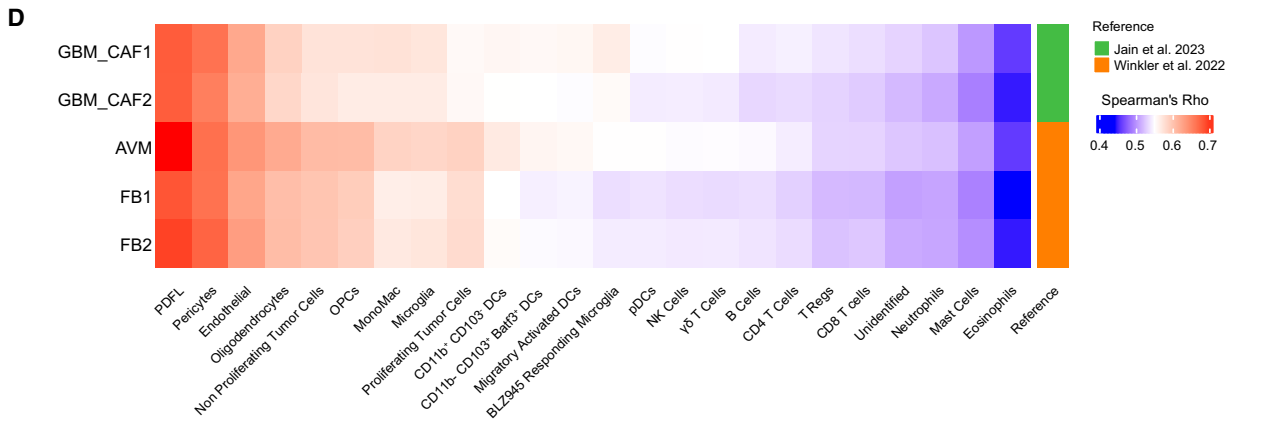

(legend on next page)

brain vasculature.[48,49] We computed a signature score comparison of DEGs in PDFLs and two reference glioblastoma CAF profiles,[48] finding a high concordance between these cell types (Figure S7B). This previous study performed pseudotime analysis and found CAFs with "early" and "late" phenotypes, potentially based on time following local activation.[48] Notably, we found that signature scores of our 7- and 14-day post-treatment PDFLs were significantly associated with the "early" phenotype vs. the "late" phenotype (Figure S7C). Pearson correlation analysis of all cell types identified in scRNA-seq of mouse PDG tumors showed that PDFLs were the most highly correlated with reference CAFs (Figure 7D). Similar studies of vascular fibroblast-like populations identified in scRNA-seq analysis of normal and adherent human vasculature[49] revealed this same correlation between mouse PDFL and human brain vascular fibroblasts (Figure S7D). Mouse PDFLs showed the highest degree of association with fibroblasts isolated from patients with arteriovenous malformations among all cell types identified in the mouse scRNA-seq data (Figures 7D and S7D). Together, these analyses indicate that the murine PDFL treatment-induced phenotype has potential human corollaries.

Inhibition of TGF-β and inflammation extends survival in preclinical BLZ945 trials

Our pathway analyses of proteomic and scRNA-seq datasets identified several pathways involved in wound healing, inflammation, EMT, and ECM production following CSF-1R inhibition (Figures 6C–6F, 7A, and 7B). Specifically, spatially resolved NicheNet analysis revealed TGF-β and pro-inflammatory cytokines as drivers of ECM-related genes in PDFLs in response to treatment perturbation of the TME (Figure 6E), suggesting that these pathways are potentially key mediators of fibrotic treatment response. We thus investigated whether targeted inhibition could eliminate this response and improve survival in preclinical trials of CSF-1R inhibition. Designing an effective treatment strategy was challenging, given that multiple cell types play a role in treatment response, likely with overlapping and redundant functions in CNS fibrosis. Due to the breadth of the biological pathways involved, and the robustness of associated wound-healing effects, we did not identify any single agent capable of complete targeted inhibition of treatment-associated fibrosis on its own (data not shown). Therefore, we instead developed a combinatorial treatment regimen specifically targeted to the most consistently upregulated pathways in our data; TGF-β signaling and generalized inflammation. Moreover, we timed the treatment intervention window (Figure 8A) to coincide with the maximal PDFL activation period identified by our temporal scRNA-seq pathway analysis.

We combined BLZ945 treatment with the corticosteroid dexamethasone (DEX) and the small molecule TGF-βRI inhibitor galunisertib (GAL), each of which has been previously employed for treatment of glioblastoma.[50–52] Neither DEX nor GAL treatment was found to have any anti-glioma efficacy as a single agent in our preclinical trials (data not shown). We next treated PDG-bearing mice with BLZ945 alone, in combination with DEX, GAL, or the triple combination (BDG), and analyzed the treated lesions during the dormancy phase at 28 days of treatment (Figure 8B). The inclusion of either DEX or GAL had no significant impact on BLZ945-mediated tumor regression or treatment-associated fibrosis (Figures 8B–8D). However, the BDG triple combination resulted in a pronounced and significant inhibition of treatment-induced fibrosis as defined by machine-learning annotation of ECM fibrosis regions, and a significant reduction in the total number of remaining tumor cells (Figures 8B–8D). We repeated this trial in the RCAS PDGFB p53 knockdown model (p53-PDG), a different glioma model with a distinct TME, which also incorporated GFP labeling of transformed tumor cells.[10,11,53] p53-PDG gliomas demonstrated a highly similar fibrotic response to BLZ945 at 28 days post-treatment, and a comparable reduction in fibrosis and the number of remaining tumor cells in response to the BDG triple combination (Figures 8E and 8F).

Based on these findings, we initiated a long-term preclinical trial with the BDG combination in the PDG tumor model. The treatment regimen consisted of daily BLZ945 combined with twice-daily treatment of GAL (50 mg/kg) for only the first 10 days, and 1 mg/kg DEX for 14 days, followed by progressive tapering-off of DEX over the next 14 days. Another critical aspect of timing DEX and GAL to only the early intervention window of treatment-induced fibrosis was that it avoided the potential issues of toxicity with long-term combinations of these drugs.

Long-term preclinical trials consisted of BLZ945 alone, DEX with GAL (DG), BLZ945 + DEX, BLZ945 + GAL, and the triple BDG combination. In the absence of BLZ945, the DG combination resulted in rapid tumor progression and morbidity in the first weeks of the trial (Figure 8G). The combinations of BLZ945 + DEX or BLZ945 + GAL showed no statistically significant difference versus the BLZ945-alone treatment arm. By contrast, the triple BDG combination cohorts showed significantly improved survival compared to BLZ945 alone, with only a single animal showing a recurrent tumor throughout this months-long study. These data strongly support the hypothesis that the fibrotic treatment effect, and the associated protective spatial niche, play a pro-tumoral role in glioblastoma survival and recurrence following treatment, and that inhibition of this response can markedly improve therapeutic efficacy.

Figure 7. Activation and dynamics of PDFL cells in post-treatment tumors

(A) Circos plot of NicheNet cell communication derived from scRNA-seq analysis between sender cells in all spatial regions, and PDFLs determined to reside in the fibrotic niche of 7-day post-BLZ945 treated lesions. Red arrows indicate target genes increased in 7-day PDFLs ($n = 3$) compared to untreated PDFLs ($n = 3$).

(B) Overrepresentation analysis (ORA) of top 200 genes upregulated in PDFLs from 7-day BLZ945-treated tumors versus untreated tumors (top), and downregulated genes in 14-day-treated versus 7-day-treated (bottom). Analysis employed Hallmark and Reactome databases.

(C) Gene signatures of genes significantly enhanced in 7B (top) involved in EMT, ECM, IFNγ, and IFNα pathways. Average log fold-change for each gene signature in PDFLs shown for each treatment time point.

(D) Heatmap of Spearman's correlation of mouse PDFL gene signature compared to publicly available scRNA-seq data for human brain vascular fibroblasts in the glioblastoma setting (Jain et al., JCI 2023) and malformed vascular setting.[49]

See also Figure S7 and Table S7.

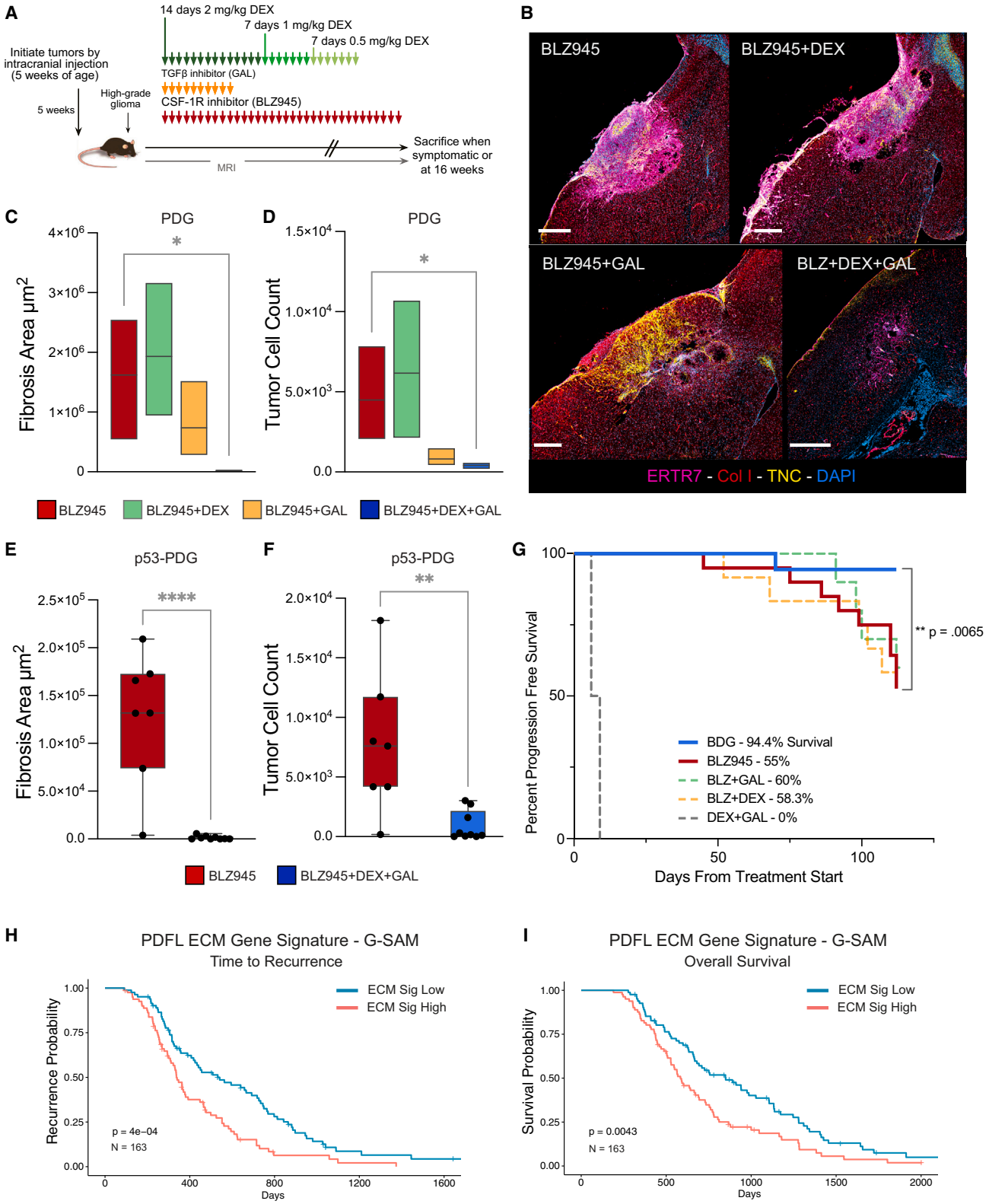

(legend on next page)

To investigate whether the fibrotic treatment response is also implicated in patient outcomes, we applied our PDFL treatment-response gene signature for ECM-related genes (Table S7) to transcriptomic data of recurrent patient glioblastomas. Stratification of 163 recurrent patient samples from the European Organisation for Research and Treatment of Cancer (EORTC) Study 1542, Glioblastoma, Stability of Actionable Mutations (G-SAM)[21] into high or low expression of the PDFL ECM gene signature demonstrated that recurrent tumors with a high ECM gene signature were associated with significantly shorter relapse times (Figure 8H). Moreover, this same stratification also showed that high ECM gene signature expression at recurrence was associated with significantly shorter overall survival (Figure 8I).

These data, along with analyses in Figure 7D further support the concept that fibrotic treatment effect in patients is connected to the activity of PDFLs or other related fibrotic cells, and that this adaptive response to anti-glioma therapy is associated with, or potentially promoting, tumor recurrence.

DISCUSSION

In this study, we employed a comprehensive orthogonal multi-omics strategy to robustly analyze the post-treatment glioblastoma microenvironment. Collectively, our data indicate that anti-glioma therapies that aggressively perturb the glioblastoma TME, such as immunotherapy, radiotherapy, and surgery, have the potential to trigger a fibrotic treatment response. Additionally, recurrent tumor growth was ubiquitously observed in direct association with fibrotic regions, which were also enriched in diverse mitogenic, neoangiogenic, and other growth-promoting signaling factors. These findings align with observations made in the clinical setting, where glioblastomas most commonly recur immediately adjacent to the site of the original lesion or the resection cavity[54,55] and are considered to be more aggressive compared to the primary tumor. Moreover, our pathological assessment of primary and recurrent glioblastoma patient samples herein revealed that fibrosis was observed significantly more frequently in recurrent disease than in primary tumor lesions. In-depth immunofluorescence imaging analysis of recurrent patient samples revealed a dense deposition of collagens and TNC near sites of prior treatment, consistent with our results in mouse models. These findings are further supported by analysis of patient transcriptomic data, which showed that cell signatures of post-treatment mouse PDFLs were correlated with faster time-to-recurrence, and worse overall prognosis. These alterations may be similar to the radiological phenomenon of ''treatment-effects,'' which are treatment-related changes visible by MRI.[56–58] The molecular basis for this so-called treatment effect is currently unknown, but our data suggest that, at least in some cases, treatment-induced scars may be the origin of the observed radiological changes.

Our data also suggest that PDFLs are a key mediator of treatment-induced CNS scarring. Time course imaging data suggest that PDFLs associated with post-treatment fibrosis originate from the glioma perivascular niche, proliferate, and differentiate into fibroblast-like cells, similar to observations made in other brain and spinal cord lesions.[27,59] These cells then migrate across the lesion responding to treatment, producing the fibrotic ECM that forms the protective niche for surviving tumor cells. However, the definitive lineage origin of these cells is currently challenging to determine since different perivascular cell types that have been described show similar expression profiles and anatomical localization,[14,35,60] including meningeal fibroblasts, type A pericytes, perivascular fibroblasts, and myeloid-derived fibrocytes. PDFLs were observed in post-treatment tumors in multiple anatomic locations, both proximal to and distant from the meninges in the prefrontal cortex, and in the hippocampal HRas-GFAP-Cre tumors, suggesting that PDFLs are distinct from meningeal fibroblasts. Moreover, high expression of fibroblast-associated genes in PDFLs, such as *Col1a1*, *Col6a1*, *Dcn*, *Lum*, and *Tnc*, but not canonical pericyte genes (*Kcnj8*, *Higd1b*, and *Rgs5*), suggests that they are different from pericytes. However, all cells were collected from the pre- or post-treatment TME, not from homeostatic conditions, making identification of cellular origin challenging. Future research to definitively isolate and define CNS perivascular cell types could aid in identifying further actionable targets to inhibit glioma treatment-associated fibrosis.

In this study, we focused on the use of a small-molecule anti-CSF-1R inhibitor for glioblastoma treatment primarily due to its potent efficacy in preclinical trials. BLZ945 is in phase I/II clinical trials for patients with solid tumors, including glioblastoma (https://doi.org/10.1158/1538-7445.AM2020-CT171), and is also in phase II trials for the treatment of the neurological disease amyotrophic lateral sclerosis (NCT04066244). Anti-CSF-1R inhibitors are more effective in tumors that contain abundant macrophages, which can be further enhanced by prior IR treatment.[12] Identification and inhibition of the potential resistance mechanisms to

Figure 8. Inhibition of treatment-associated fibrosis extends survival in preclinical anti-CSF-1R trials

(A) Schematic of preclinical treatment regimen for murine model of PDGFB-driven glioblastoma treated with BLZ945, the TGF-beta inhibitor galunisertib (GAL) and dexamethasone (DEX).

(B) Representative IF images of PDG samples treated for 28 days with BLZ945, BLZ945 + DEX (BD), BLZ945 + GAL (BG), and BLZ945 + DEX + GAL (BDG). PDFLs labeled with ER-TR7, fibrosis labeled with Col I and TNC. Scale bars: 500 μm.

(C) Quantification of regions annotated as fibrotic ECM in 28-day PDG samples for each treatment condition ($n = 3$). One-tailed t test $^{*}p = 0.0259$. Boxplots show median, upper and lower quartile, whiskers show upper and lower extreme, datapoints and outliers shown as dots.

(D) Total count of tumor cells in 28-day PDG samples for each treatment condition ($n = 3$). One-tailed t test $^{*}p = 0.0392$.

(E) Quantification of regions annotated as fibrotic ECM in 28-day p53-PDG samples treated with BLZ945 ($n = 7$) and BDG ($n = 9$). One-tailed t test $^{****}p < 0.0001$.

(F) Total count of Tumor cells in 28-day p53-PDG samples treated with BLZ945 ($n = 7$) and BDG ($n = 9$). One-tailed t test $^{**}p = 0.002$.

(G) Kaplan-Meier curves of BLZ945 + vehicle ($n = 20$) DEX + GAL ($n = 6$), BDG ($n = 18$), BD ($n = 12$), and BG ($n = 10$) treated mice bearing high-grade PDG tumors (log rank Mantel-Cox test). All-versus-all comparison between treatment groups, $p < 0.0001$. DEX + GAL compared to BLZ945 + vehicle, $p < 0.0001$. BDG compared to BLZ945 + vehicle, $p = 0.0065$.

(H and I) Kaplan-Meier survival analysis of recurrent patient gliomas from G-SAM consortium stratified by high and low expression of the PDFL ECM treatment response gene signature.

anti-CSF-1R therapy may thus have important future clinical applications. Our findings herein notably indicate that addressing treatment-associated fibrosis in the patient setting could improve the efficacy of multiple treatment modalities, including surgical resection and IR treatment, as these both stimulated fibrotic treatment responses. However, not all modes of CNS damage can be considered equivalent, and different sources of perturbation may elicit varying environmental responses.[27] While several key features of fibrotic treatment response were shared between anti-CSF-1R treatment, surgical resection, and IR therapy in our models, they also differed in the duration of dormancy, the extent of tumor regression, and the levels of immune cell infiltration. These differential responses to damage will likely require anti-fibrosis treatments tailored to the type of perturbation. While the use of dexamethasone in combination with galunisertib successfully inhibited anti-CSF-1R treatment-induced fibrosis, dexamethasone was previously shown to negatively impact survival in PDG tumors treated with IR therapy,[61] and thus may not be well suited for this particular perturbation. A potential reason may be the immune-suppressive effects of dexamethasone that, in this specific scenario, inhibits the immunogenicity of IR therapy.[61] In our study, we designed an anti-fibrosis treatment regimen specifically tailored for anti-CSF-1R mediated fibrosis, a therapy that re-educates the TME.[22] While this may be translatable to other anti-glioma therapies, future studies to improve SoC efficacy should additionally focus on mechanisms specific to those treatments.

Enriched fibrotic treatment response gene signatures in patients treated with SoC therapy were found to be significantly associated with faster relapse and decreased survival, irrespective of other clinical factors. Since prognostic gene signatures were explicitly derived from PDFLs, these results suggest that fibroblast-like cells may also be key mediators of fibrotic response following treatment in patients and mouse models. This implies that therapeutic targeting of fibroblasts or fibrotic treatment effects could be an important strategy for extending the benefit of SoC glioblastoma treatment. Our data also show increased accumulation of T cells in areas of fibrosis in close association with surviving cancer cells. However, these T cells expressed exhausted phenotypes, supporting the clinical strategy of evaluating combinatorial anti-CSF-1R inhibition with immune checkpoint inhibitors following SoC treatment (https://doi.org/10.1158/1538-7445.AM2020-CT171). An important consideration when designing future clinical trials is the timing and order in which different drugs will be used. Our data suggest that, when targeting treatment-associated fibrosis, there is only a short therapeutic window. CNS scars develop very rapidly after treatment initiation and breaking down a mature scar may be considerably more challenging than preventing scar formation. Moreover, inhibiting an immune response using dexamethasone may have adverse effects in the long term, especially when using therapies that depend on immune activation such as CAR T cells. Finally, in addition to providing therapeutic targets, the cellular organization and super-structures associated with the fibrotic treatment effect could serve as prognostic features for therapeutic response.

Limitations of the study

It is currently unknown how the post-treatment fibrotic niche promotes dormancy and stemness in resident glioblastoma cells. Recent studies in extracranial tumors have found that dormancy can be promoted via collagen III signaling through DDR1/STAT1,[20] which we also found to be highly expressed in treatment-induced CNS scarring. This is an especially interesting mechanistic question, as our study and several others show that areas of fibrosis are high in potentially growth promoting signals, yet glioblastoma cells were found to remain dormant within fibrosis for several months. If these scars drive glioma dormancy, another interesting question is how the surviving tumor cells in this niche regain proliferative capacity. In rebound tumor models, even in early stages, proliferating tumor cells are found directly adjacent to the scar in the brain parenchyma, and have gene expression profiles similar to dormant cells within the fibrotic niche, suggesting that glioblastoma cells must first escape from the fibrotic niche before switching to a proliferative phenotype. This may occur through active or stochastic cell migration or through the breakdown of the fibrotic scar via ECM remodeling. Further studies exploring the precise mechanisms and dynamics of ECM-mediated glioma dormancy and escape could reveal additional therapeutic strategies to exploit treatment-associated fibrosis to extend post-treatment dormancy.

A limitation in studying the impact of treatment-induced fibrosis in the patient setting is the potential under-sampling of fibrotic regions in surgical resections, and the possible loss of fibroblast-like populations due to standard dissociation techniques for single-cell analysis. More focused sample collection, and single-cell *in situ* spatial transcriptomics combined with customized HIFI panels would enrich single-cell omics analyses of fibrotic niches in patient samples. This challenge limited the scope of our study in exhaustively addressing the molecular impact of dexamethasone and galunisertib treatment on the TME. Advances in larger gene panels for *in situ* spatial transcriptomic platforms would empower future studies to address the multivariate impacts of targeted anti-fibrosis treatments.

A potential limitation in translating the anti-fibrosis strategies employed in this study to clinical treatment of glioblastoma is the use of the corticosteroid dexamethasone. In our model system, the broad activity of dexamethasone was beneficial in targeting the highly pleiotropic neuroinflammation pathways activated following treatment with anti-CSF-1R treatment. However, dexamethasone also has immunosuppressive effects in the patient setting, and so has potentially detrimental interactions with therapeutic strategies that do not target immune cells in a manner similar to anti-CSF-1R treatment. Further research into the precise mechanistic role of inflammatory pathways in treatment-associated fibrosis can identify better targeted therapeutics against specific inflammatory pathways following different types of treatment interventions.

RESOURCE AVAILABILITY

Lead contact

Further information and requests for resources and reagents should be directed to and will be fulfilled by the lead contact, Johanna Joyce (johanna.joyce@unil.ch).

Material availability

Requests for resources and reagents should be directed to and will be fulfilled by the lead contact, Johanna Joyce (johanna.joyce@unil.ch).

Data and code availability

All code, models, and underlying data are available upon request. HIFI image data are available upon request. scRNA-seq data are available via the NCBI GEO repository, accession number GSE229409. The mass spectrometry proteomics data have been deposited to the ProteomeXchange Consortium via the PRIDE[80] partner repository with the dataset identifier PXD041689. Xenium spatial transcriptomic data are available via the NCBI GEO repository, accession number GSE266969. The combined scRNA-seq and Xenium data are available as a SuperSeries via the NCBI GEO repository, accession number GSE266971. Any additional data reported in this paper is available from the lead contact upon reasonable request.

ACKNOWLEDGMENTS

We gratefully acknowledge all current and former members of the Joyce lab for insightful discussions and advice, and assistance with mouse experiments, particularly Leire Bejarano, Paola Guerrero Aruffo, Marta Jordao, and Rui Santalla Mendez. We thank Véronique Noguet Brechbühl (Mouse Pathology Facility, AGORA/FBM) for sectioning of pathological samples; members of the UNIL Protein Analysis Facility for acquiring the mass spectrometry proteomic data; Danny Labes and the UNIL Flow Cytometry Facility for assistance with cell sorting; and Chiara Bastiancich for training in cranial surgical resection of murine brain tumors. Sylvie Andre and Marina Alexandre Gaveta generously provided their time and expertise in processing samples for spatial transcriptomics. We would like to acknowledge the Agora In Vivo Center and In Vivo Imaging Facility for their contributions to animal care. BLZ945 was provided free of charge by Novartis. Data from the G-SAM public dataset were generously provided by the lab of Prof. Pim J. French. This research was funded by The Brain Tumour Charity Future Leaders Fellowship (JF_2022_10659) and The Brian Cross Memorial Trust (S.S.W.); a Human Frontier Science Program fellowship (LT000240/2017-L) and a Veni fellowship from the Netherlands Organisation for Scientific Research (09150161910076) (A.Z.); Swiss Cancer Research (KFS-3390-08-2016 and KFS-5280-02-2021; J.A.J.), University of Lausanne (J.A.J.), Charlie Teo Foundation (J.A.J.), Ludwig Institute for Cancer Research (J.A.J. and D.H.), The Fondation Sante (Belmont-sur-Lausanne) and The Anna Fuller Fund (A.C. and D.H.).

AUTHOR CONTRIBUTIONS

S.S.W., A.Z., and J.A.J. conceived the study, designed experiments, and interpreted data. S.S.W. and A.Z. performed the experiments with assistance from A.C., P.A., S.A., D.H., D.C., and K.H. S.S.W. and A.Z. performed all experimental analyses. S.S.W., N.F., J.L., and S.N. performed the computational analyses. M.Q. performed mass spectrometry experiments. E.A., M.L.D.B., R.T.D., M.E.H., G.C., and A.F.H. provided clinical information and material. J.T.H. performed histopathological review. S.S.W., A.Z., and J.A.J. wrote the manuscript. S.S.W. and A.Z. prepared the figures. J.A.J. supervised the research. All authors reviewed and approved the manuscript.

DECLARATION OF INTERESTS

A.Z. is a current employee of Genmab; D.C. received consulting fees from Seed Biosciences S.A. and is a current employee of Novigenix; S.N. is a current employee of Roche Pharmaceuticals; A.F.H. has served on advisory boards and speaker's bureau for Novocure and Bayer; M.E.H. has an advisory role at TME Pharma; J.A.J. received a speaker honorarium from Bristol Meyers Squibb, and served on the scientific advisory board of Pionyr Immunotherapeutics; J.A.J. and D.H. serve on the *Cancer Cell* editorial advisory board.

STAR★METHODS

Detailed methods are provided in the online version of this paper and include the following:

SUPPLEMENTAL INFORMATION

Supplemental information can be found online at https://doi.org/10.1016/j.ccell.2024.08.012.

Received: June 21, 2023
Revised: June 6, 2024
Accepted: August 12, 2024
Published: September 9, 2024

REFERENCES

1. Ostrom, Q.T., Gittleman, H., Farah, P., Ondracek, A., Chen, Y., Wolinsky, Y., Stroup, N.E., Kruchko, C., and Barnholtz-Sloan, J.S. (2013). CBTRUS statistical report: Primary brain and central nervous system tumors diagnosed in the United States in 2006-2010. Neuro Oncol. *15*. ii1–56. https://doi.org/10.1093/neuonc/not151.
2. Stupp, R., Hegi, M.E., Mason, W.P., van den Bent, M.J., Taphoorn, M.J.B., Janzer, R.C., Ludwin, S.K., Allgeier, A., Fisher, B., Belanger, K., et al. (2009). Effects of radiotherapy with concomitant and adjuvant temozolomide versus radiotherapy alone on survival in glioblastoma in a randomised phase III study: 5-year analysis of the EORTC-NCIC trial. Lancet Oncol. *10*, 459–466. https://doi.org/10.1016/S1470-2045(09)70025-7.
3. Yabo, Y.A., Niclou, S.P., and Golebiewska, A. (2022). Cancer cell heterogeneity and plasticity: A paradigm shift in glioblastoma. Neuro Oncol. *24*, 669–682. https://doi.org/10.1093/neuonc/noab269.
4. De Silva, M.I., Stringer, B.W., and Bardy, C. (2023). Neuronal and tumourigenic boundaries of glioblastoma plasticity. Trends Cancer *9*, 223–236. https://doi.org/10.1016/j.trecan.2022.10.010.
5. Klemm, F., Maas, R.R., Bowman, R.L., Kornete, M., Soukup, K., Nassiri, S., Brouland, J.P., Iacobuzio-Donahue, C.A., Brennan, C., Tabar, V., et al. (2020). Interrogation of the Microenvironmental Landscape in Brain Tumors Reveals Disease-Specific Alterations of Immune Cells. Cell *181*, 1643–1660.e17. https://doi.org/10.1016/j.cell.2020.05.007.
6. Komohara, Y., Ohnishi, K., Kuratsu, J., and Takeya, M. (2008). Possible involvement of the M2 anti-inflammatory macrophage phenotype in growth of human gliomas. J. Pathol. *216*, 15–24. https://doi.org/10.1002/path.2370.
7. Hussain, S.F., Yang, D., Suki, D., Aldape, K., Grimm, E., and Heimberger, A.B. (2006). The role of human glioma-infiltrating microglia/macrophages in mediating antitumor immune responses. Neuro Oncol. *8*, 261–279. https://doi.org/10.1215/15228517-2006-008.
8. Ruffell, B., and Coussens, L.M. (2015). Macrophages and therapeutic resistance in cancer. Cancer Cell *27*, 462–472. https://doi.org/10.1016/j.ccell.2015.02.015.

9. Ries, C.H., Hoves, S., Cannarile, M.A., and Rüttinger, D. (2015). CSF-1/CSF-1R targeting agents in clinical development for cancer therapy. Curr. Opin. Pharmacol. *23*, 45–51. https://doi.org/10.1016/j.coph.2015.05.008.

10. Quail, D.F., Bowman, R.L., Akkari, L., Quick, M.L., Schuhmacher, A.J., Huse, J.T., Holland, E.C., Sutton, J.C., and Joyce, J.A. (2016). The tumor microenvironment underlies acquired resistance to CSF-1R inhibition in gliomas. Science *352*, aad3018. https://doi.org/10.1126/science.aad3018.

11. Zomer, A., Croci, D., Kowal, J., van Gurp, L., and Joyce, J.A. (2022). Multimodal imaging of the dynamic brain tumor microenvironment during glioblastoma progression and in response to treatment. iScience *25*, 104570. https://doi.org/10.1016/j.isci.2022.104570.

12. Akkari, L., Bowman, R.L., Tessier, J., Klemm, F., Handgraaf, S.M., de Groot, M., Quail, D.F., Tillard, L., Gadiot, J., Huse, J.T., et al. (2020). Dynamic changes in glioma macrophage populations after radiotherapy reveal CSF-1R inhibition as a strategy to overcome resistance. Sci. Transl. Med. *12*, eaaw7843. https://doi.org/10.1126/scitranslmed.aaw7843.

13. Yan, D., Kowal, J., Akkari, L., Schuhmacher, A.J., Huse, J.T., West, B.L., and Joyce, J.A. (2017). Inhibition of colony stimulating factor-1 receptor abrogates microenvironment-mediated therapeutic resistance in gliomas. Oncogene *36*, 6049–6058. https://doi.org/10.1038/onc.2017.261.

14. Dorrier, C.E., Jones, H.E., Pintarić, L., Siegenthaler, J.A., and Daneman, R. (2022). Emerging roles for CNS fibroblasts in health, injury and disease. Nat. Rev. Neurosci. *23*, 23–34. https://doi.org/10.1038/s41583-021-00525-w.

15. Kalluri, R. (2016). The biology and function of fibroblasts in cancer. Nat. Rev. Cancer *16*, 582–598. https://doi.org/10.1038/nrc.2016.73.

16. Chandler, C., Liu, T., Buckanovich, R., and Coffman, L.G. (2019). The double edge sword of fibrosis in cancer. Transl. Res. *209*, 55–67. https://doi.org/10.1016/j.trsl.2019.02.006.

17. Sala, M., Ros, M., and Saltel, F. (2020). A Complex and Evolutive Character: Two Face Aspects of ECM in Tumor Progression. Front. Oncol. *10*, 1620. https://doi.org/10.3389/fonc.2020.01620.

18. Piersma, B., Hayward, M.K., and Weaver, V.M. (2020). Fibrosis and cancer: A strained relationship. Biochim. Biophys. Acta. Rev. Cancer *1873*, 188356. https://doi.org/10.1016/j.bbcan.2020.188356.

19. Miroshnikova, Y.A., Mouw, J.K., Barnes, J.M., Pickup, M.W., Lakins, J.N., Kim, Y., Lobo, K., Persson, A.I., Reis, G.F., McKnight, T.R., et al. (2016). Tissue mechanics promote IDH1-dependent HIF1alpha-tenascin C feedback to regulate glioblastoma aggression. Nat. Cell Biol. *18*, 1336–1345. https://doi.org/10.1038/ncb3429.

20. Di Martino, J.S., Nobre, A.R., Mondal, C., Taha, I., Farias, E.F., Fertig, E.J., Naba, A., Aguirre-Ghiso, J.A., and Bravo-Cordero, J.J. (2022). A tumor-derived type III collagen-rich ECM niche regulates tumor cell dormancy. Nat. Can. (Ott.) *3*, 90–107. https://doi.org/10.1038/s43018-021-00291-9.

21. Hoogstrate, Y., Draaisma, K., Ghisai, S.A., van Hijfte, L., Barin, N., de Heer, I., Coppieters, W., van den Bosch, T.P.P., Bolleboom, A., Gao, Z., et al. (2023). Transcriptome analysis reveals tumor microenvironment changes in glioblastoma. Cancer Cell *41*, 678–692.e7. https://doi.org/10.1016/j.ccell.2023.02.019.

22. Pyonteck, S.M., Akkari, L., Schuhmacher, A.J., Bowman, R.L., Sevenich, L., Quail, D.F., Olson, O.C., Quick, M.L., Huse, J.T., Teijeiro, V., et al. (2013). CSF-1R inhibition alters macrophage polarization and blocks glioma progression. Nat. Med. *19*, 1264–1272. https://doi.org/10.1038/nm.3337.

23. Hambardzumyan, D., Amankulor, N.M., Helmy, K.Y., Becher, O.J., and Holland, E.C. (2009). Modeling Adult Gliomas Using RCAS/t-va Technology. Transl. Oncol. *2*, 89–95.

24. Becker, H., Castaneda-Vega, S., Patzwaldt, K., Przystal, J.M., Walter, B., Michelotti, F.C., Canjuga, D., Tatagiba, M., Pichler, B., Beck, S.C., et al. (2022). Multiparametric Longitudinal Profiling of RCAS-tva-Induced PDGFB-Driven Experimental Glioma. Brain Sci. *12*, 1426. https://doi.org/10.3390/brainsci12111426.

25. Dias, D.O., and Göritz, C. (2018). Fibrotic scarring following lesions to the central nervous system. Matrix Biol. *68–69*, 561–570. https://doi.org/10.1016/j.matbio.2018.02.009.

26. Cregg, J.M., DePaul, M.A., Filous, A.R., Lang, B.T., Tran, A., and Silver, J. (2014). Functional regeneration beyond the glial scar. Exp. Neurol. *253*, 197–207. https://doi.org/10.1016/j.expneurol.2013.12.024.

27. Dias, D.O., Kalkitsas, J., Kelahmetoglu, Y., Estrada, C.P., Tatarishvili, J., Holl, D., Jansson, L., Banitalebi, S., Amiry-Moghaddam, M., Ernst, A., et al. (2021). Pericyte-derived fibrotic scarring is conserved across diverse central nervous system lesions. Nat. Commun. *12*, 5501. https://doi.org/10.1038/s41467-021-25585-5.

28. Friedmann-Morvinski, D., Bushong, E.A., Ke, E., Soda, Y., Marumoto, T., Singer, O., Ellisman, M.H., and Verma, I.M. (2012). Dedifferentiation of neurons and astrocytes by oncogenes can induce gliomas in mice. Science *338*, 1080–1084. https://doi.org/10.1126/science.1226929.

29. Chryplewicz, A., Scotton, J., Tichet, M., Zomer, A., Shchors, K., Joyce, J.A., Homicsko, K., and Hanahan, D. (2022). Cancer cell autophagy, reprogrammed macrophages, and remodeled vasculature in glioblastoma triggers tumor immunity. Cancer Cell *40*, 1111–1127.e9. https://doi.org/10.1016/j.ccell.2022.08.014.

30. Watson, S.S., Duc, B., Kang, Z., de Tonnac, A., Eling, N., Font, L., Whitmarsh, T., Massara, M.; iMAXT Consortium, and Bodenmiller, B., et al. (2024). Microenvironmental reorganization in brain tumors following radiotherapy and recurrence revealed by hyperplexed immunofluorescence imaging. Nat. Commun. *15*, 3226. https://doi.org/10.1038/s41467-024-47185-9.

31. Bejarano, L., Kauzlaric, A., Lamprou, E., Lourenco, J., Fournier, N., Ballabio, M., Colotti, R., Maas, R., Galland, S., Massara, M., et al. (2024). Interrogation of endothelial and mural cells in brain metastasis reveals key immune-regulatory mechanisms. Cancer Cell *42*, 378–395.e10. https://doi.org/10.1016/j.ccell.2023.12.018.

32. Crouch, E.E., and Doetsch, F. (2018). FACS isolation of endothelial cells and pericytes from mouse brain microregions. Nat. Protoc. *13*, 738–751. https://doi.org/10.1038/nprot.2017.158.

33. Ke, R., Mignardi, M., Pacureanu, A., Svedlund, J., Botling, J., Wählby, C., and Nilsson, M. (2013). In situ sequencing for RNA analysis in preserved tissue and cells. Nat. Methods *10*, 857–860. https://doi.org/10.1038/nmeth.2563.

34. Janesick, A., Shelansky, R., Gottscho, A.D., Wagner, F., Williams, S.R., Rouault, M., Beliakoff, G., Morrison, C.A., Oliveira, M.F., Sicherman, J.T., et al. (2023). High resolution mapping of the tumor microenvironment using integrated single-cell, spatial and in situ analysis. Nat. Commun. *14*, 8353. https://doi.org/10.1038/s41467-023-43458-x.

35. Dorrier, C.E., Aran, D., Haenelt, E.A., Sheehy, R.N., Hoi, K.K., Pintarić, L., Chen, Y., Lizama, C.O., Cautivo, K.M., Weiner, G.A., et al. (2021). CNS fibroblasts form a fibrotic scar in response to immune cell infiltration. Nat. Neurosci. *24*, 234–244. https://doi.org/10.1038/s41593-020-00770-9.

36. Goritz, C., Dias, D.O., Tomilin, N., Barbacid, M., Shupliakov, O., and Frisen, J. (2011). A pericyte origin of spinal cord scar tissue. Science *333*, 238–242. https://doi.org/10.1126/science.1203165.

37. Windhager, J., Bodenmiller, B., and Eling, N. (2021). An end-to-end workflow for multiplexed image processing and analysis. Preprint at bioRxiv. https://doi.org/10.1101/2021.11.12.468357.

38. Rusu, P., Shao, C., Neuerburg, A., Acikgöz, A.A., Wu, Y., Zou, P., Phapale, P., Shankar, T.S., Döring, K., Dettling, S., et al. (2019). GPD1 Specifically Marks Dormant Glioma Stem Cells with a Distinct Metabolic Profile. Cell Stem Cell *25*, 241–257.e8. https://doi.org/10.1016/j.stem.2019.06.004.

39. Zbinden, M., Duquet, A., Lorente-Trigos, A., Ngwabyt, S.N., Borges, I., and Ruiz i Altaba, A. (2010). NANOG regulates glioma stem cells and is essential in vivo acting in a cross-functional network with GLI1 and p53. EMBO J. *29*, 2659–2674. https://doi.org/10.1038/emboj.2010.137.

40. Aldaz, P., Martin-Martin, N., Saenz-Antonanzas, A., Carrasco-Garcia, E., Alvarez-Satta, M., Elua-Pinin, A., Pollard, S.M., Lawrie, C.H., Moreno-Valladares, M., Sampron, N., et al. (2022). High SOX9 Maintains Glioma

Stem Cell Activity through a Regulatory Loop Involving STAT3 and PML. Int. J. Mol. Sci. *23*, 4511. https://doi.org/10.3390/ijms23094511.

41. Bao, S., Wu, Q., McLendon, R.E., Hao, Y., Shi, Q., Hjelmeland, A.B., Dewhirst, M.W., Bigner, D.D., and Rich, J.N. (2006). Glioma stem cells promote radioresistance by preferential activation of the DNA damage response. Nature *444*, 756–760. https://doi.org/10.1038/nature05236.
42. Zhu, Z., Khan, M.A., Weiler, M., Blaes, J., Jestaedt, L., Geibert, M., Zou, P., Gronych, J., Bernhardt, O., Korshunov, A., et al. (2014). Targeting self-renewal in high-grade brain tumors leads to loss of brain tumor stem cells and prolonged survival. Cell Stem Cell *15*, 185–198. https://doi.org/10.1016/j.stem.2014.04.007.
43. Shechter, R., and Schwartz, M. (2013). CNS sterile injury: just another wound healing? Trends Mol. Med. *19*, 135–143. https://doi.org/10.1016/j.molmed.2012.11.007.
44. Adams, K.L., and Gallo, V. (2018). The diversity and disparity of the glial scar. Nat. Neurosci. *21*, 9–15. https://doi.org/10.1038/s41593-017-0033-9.
45. Andreatta, M., Corria-Osorio, J., Müller, S., Cubas, R., Coukos, G., and Carmona, S.J. (2021). Interpretation of T cell states from single-cell transcriptomics data using reference atlases. Nat. Commun. *12*, 2965. https://doi.org/10.1038/s41467-021-23324-4.
46. Browaeys, R., Saelens, W., and Saeys, Y. (2020). NicheNet: modeling intercellular communication by linking ligands to target genes. Nat. Methods *17*, 159–162. https://doi.org/10.1038/s41592-019-0667-5.
47. Di Gregorio, J., Robuffo, I., Spalletta, S., Giambuzzi, G., De Iuliis, V., Toniato, E., Martinotti, S., Conti, P., and Flati, V. (2020). The Epithelial-to-Mesenchymal Transition as a Possible Therapeutic Target in Fibrotic Disorders. Front. Cell Dev. Biol. *8*, 607483. https://doi.org/10.3389/fcell.2020.607483.
48. Jain, S., Rick, J.W., Joshi, R.S., Beniwal, A., Spatz, J., Gill, S., Chang, A.C.C., Choudhary, N., Nguyen, A.T., Sudhir, S., et al. (2023). Single-cell RNA sequencing and spatial transcriptomics reveal cancer-associated fibroblasts in glioblastoma with protumoral effects. J. Clin. Invest. *133*, e147087. https://doi.org/10.1172/JCI147087.
49. Winkler, E.A., Kim, C.N., Ross, J.M., Garcia, J.H., Gil, E., Oh, I., Chen, L.Q., Wu, D., Catapano, J.S., Raygor, K., et al. (2022). A single-cell atlas of the normal and malformed human brain vasculature. Science *375*, eabi7377. https://doi.org/10.1126/science.abi7377.
50. Uhl, M., Aulwurm, S., Wischhusen, J., Weiler, M., Ma, J.Y., Almirez, R., Mangadu, R., Liu, Y.W., Platten, M., Herrlinger, U., et al. (2004). SD-208, a novel transforming growth factor beta receptor I kinase inhibitor, inhibits growth and invasiveness and enhances immunogenicity of murine and human glioma cells in vitro and in vivo. Cancer Res. *64*, 7954–7961. https://doi.org/10.1158/0008-5472.CAN-04-1013.
51. Brandes, A.A., Carpentier, A.F., Kesari, S., Sepulveda-Sanchez, J.M., Wheeler, H.R., Chinot, O., Cher, L., Steinbach, J.P., Capper, D., Specenier, P., et al. (2016). A Phase II randomized study of galunisertib monotherapy or galunisertib plus lomustine compared with lomustine monotherapy in patients with recurrent glioblastoma. Neuro Oncol. *18*, 1146–1156. https://doi.org/10.1093/neuonc/now009.
52. Afshari, A.R., Sanati, M., Aminyavari, S., Shakeri, F., Bibak, B., Keshavarzi, Z., Soukhtanloo, M., Jalili-Nik, M., Sadeghi, M.M., Mollazadeh, H., et al. (2022). Advantages and drawbacks of dexamethasone in glioblastoma multiforme. Crit. Rev. Oncol. Hematol. *172*, 103625. https://doi.org/10.1016/j.critrevonc.2022.103625.
53. Ozawa, T., Riester, M., Cheng, Y.K., Huse, J.T., Squatrito, M., Helmy, K., Charles, N., Michor, F., and Holland, E.C. (2014). Most human non-GCIMP glioblastoma subtypes evolve from a common proneural-like precursor glioma. Cancer Cell *26*, 288–300. https://doi.org/10.1016/j.ccr.2014.06.005.
54. Rapp, M., Baernreuther, J., Turowski, B., Steiger, H.J., Sabel, M., and Kamp, M.A. (2017). Recurrence Pattern Analysis of Primary Glioblastoma. World Neurosurg. *103*, 733–740. https://doi.org/10.1016/j.wneu.2017.04.053.
55. Jiang, H., Yu, K., Li, M., Cui, Y., Ren, X., Yang, C., Zhao, X., and Lin, S. (2020). Classification of Progression Patterns in Glioblastoma: Analysis of Predictive Factors and Clinical Implications. Front. Oncol. *10*, 590648. https://doi.org/10.3389/fonc.2020.590648.
56. Himes, B.T., Arnett, A.L., Merrell, K.W., Gates, M.J., Bhargav, A.G., Raghunathan, A., Brown, D.A., Burns, T.C., and Parney, I.F. (2020). Glioblastoma Recurrence Versus Treatment Effect in a Pathology-Documented Series. Can. J. Neurol. Sci. *47*, 525–530. https://doi.org/10.1017/cjn.2020.36.
57. Parvez, K., Parvez, A., and Zadeh, G. (2014). The diagnosis and treatment of pseudoprogression, radiation necrosis and brain tumor recurrence. Int. J. Mol. Sci. *15*, 11832–11846. https://doi.org/10.3390/ijms150711832.
58. Clarke, J.L., and Chang, S. (2009). Pseudoprogression and pseudoresponse: challenges in brain tumor imaging. Curr. Neurol. Neurosci. Rep. *9*, 241–246. https://doi.org/10.1007/s11910-009-0035-4.
59. Rentsch, N.H., and Rust, R. (2022). Scary' pericytes: the fibrotic scar in brain and spinal cord lesions. Trends Neurosci. *45*, 6–7. https://doi.org/10.1016/j.tins.2021.10.013.
60. Ayazi, M., Zivkovic, S., Hammel, G., Stefanovic, B., and Ren, Y. (2022). Fibrotic Scar in CNS Injuries: From the Cellular Origins of Fibroblasts to the Molecular Processes of Fibrotic Scar Formation. Cells *11*, 2371. https://doi.org/10.3390/cells11152371.
61. Pitter, K.L., Tamagno, I., Alikhanyan, K., Hosni-Ahmed, A., Pattwell, S.S., Donnola, S., Dai, C., Ozawa, T., Chang, M., Chan, T.A., et al. (2016). Corticosteroids compromise survival in glioblastoma. Brain *139*, 1458–1471. https://doi.org/10.1093/brain/aww046.
62. Dai, C., Celestino, J.C., Okada, Y., Louis, D.N., Fuller, G.N., and Holland, E.C. (2001). PDGF autocrine stimulation dedifferentiates cultured astrocytes and induces oligodendrogliomas and oligoastrocytomas from neural progenitors and astrocytes in vivo. Genes Dev. *15*, 1913–1925. https://doi.org/10.1101/gad.903001.
63. Becher, O.J., Hambardzumyan, D., Fomchenko, E.I., Momota, H., Mainwaring, L., Bleau, A.M., Katz, A.M., Edgar, M., Kenney, A.M., Cordon-Cardo, C., et al. (2008). Gli activity correlates with tumor grade in platelet-derived growth factor-induced gliomas. Cancer Res. *68*, 2241–2249. https://doi.org/10.1158/0008-5472.CAN-07-6350.
64. Bowman, R.L., Klemm, F., Akkari, L., Pyonteck, S.M., Sevenich, L., Quail, D.F., Dhara, S., Simpson, K., Gardner, E.E., Iacobuzio-Donahue, C.A., et al. (2016). Macrophage Ontogeny Underlies Differences in Tumor-Specific Education in Brain Malignancies. Cell Rep. *17*, 2445–2459. https://doi.org/10.1016/j.celrep.2016.10.052.
65. Salmon, P., and Trono, D. (2007). Production and titration of lentiviral vectors. Curr. Protoc. Hum. Genet. Chapter 12, Unit 12 10. https://doi.org/10.1002/0471142905.hg1210s54.
66. Tchougounova, E., Kastemar, M., Bråsäter, D., Holland, E.C., Westermark, B., and Uhrbom, L. (2007). Loss of Arf causes tumor progression of PDGFB-induced oligodendroglioma. Oncogene *26*, 6289–6296. https://doi.org/10.1038/sj.onc.1210455.
67. Bianco, J., Bastiancich, C., Joudiou, N., Gallez, B., des Rieux, A., and Danhier, F. (2017). Novel model of orthotopic U-87 MG glioblastoma resection in athymic nude mice. J. Neurosci. Methods *284*, 96–102. https://doi.org/10.1016/j.jneumeth.2017.04.019.
68. Gut, G., Herrmann, M.D., and Pelkmans, L. (2018). Multiplexed protein maps link subcellular organization to cellular states. Science *361*, eaar7042. https://doi.org/10.1126/science.aar7042.
69. Bankhead, P., Loughrey, M.B., Fernández, J.A., Dombrowski, Y., McArt, D.G., Dunne, P.D., McQuaid, S., Gray, R.T., Murray, L.J., Coleman, H.G., et al. (2017). QuPath: Open source software for digital pathology image analysis. Sci. Rep. *7*, 16878. https://doi.org/10.1038/s41598-017-17204-5.
70. Schmidt, U., Weigert, M., Broaddus, C., and Myers, G. (2018). Cell Detection with Star-Convex Polygons (Springer International Publishing), pp. 265–273.

71. Csárdi, G., and Nepusz, T. (2006). The Igraph Software Package for Complex Network Research.

72. Kulak, N.A., Pichler, G., Paron, I., Nagaraj, N., and Mann, M. (2014). Minimal, encapsulated proteomic-sample processing applied to copy-number estimation in eukaryotic cells. Nat. Methods *11*, 319–324. https://doi.org/10.1038/nmeth.2834.

73. Wisniewski, J.R., and Gaugaz, F.Z. (2015). Fast and sensitive total protein and Peptide assays for proteomic analysis. Anal. Chem. *87*, 4110–4116. https://doi.org/10.1021/ac504689z.

74. Cox, J., and Mann, M. (2008). MaxQuant enables high peptide identification rates, individualized p.p.b.-range mass accuracies and proteome-wide protein quantification. Nat. Biotechnol. *26*, 1367–1372. https://doi.org/10.1038/nbt.1511.

75. Cox, J., Neuhauser, N., Michalski, A., Scheltema, R.A., Olsen, J.V., and Mann, M. (2011). Andromeda: a peptide search engine integrated into the MaxQuant environment. J. Proteome Res. *10*, 1794–1805. https://doi.org/10.1021/pr101065j.

76. Cox, J., Hein, M.Y., Luber, C.A., Paron, I., Nagaraj, N., and Mann, M. (2014). Accurate proteome-wide label-free quantification by delayed normalization and maximal peptide ratio extraction, termed MaxLFQ. Mol. Cell. Proteomics *13*, 2513–2526. https://doi.org/10.1074/mcp.M113.031591.

77. Tyanova, S., Temu, T., Sinitcyn, P., Carlson, A., Hein, M.Y., Geiger, T., Mann, M., and Cox, J. (2016). The Perseus computational platform for comprehensive analysis of (prote)omics data. Nat. Methods *13*, 731–740. https://doi.org/10.1038/nmeth.3901.

78. Zhang, X., Smits, A.H., van Tilburg, G.B., Ovaa, H., Huber, W., and Vermeulen, M. (2018). Proteome-wide identification of ubiquitin interactions using UbIA-MS. Nat. Protoc. *13*, 530–550. https://doi.org/10.1038/nprot.2017.147.

79. Baddeley, A., Rubak, E., and Turner, R. (2015). Spatial Point Patterns: Methodology and Applications with R, 1st edition (Chapman and Hall/CRC), p. 828. https://doi.org/10.1201/b19708.

80. R Core Team (2021). R: A language and environment for statistical computing (R Foundation for Statistical Computing). https://www.R-project.org/.

STAR★METHODS

KEY RESOURCES TABLE

REAGENT or RESOURCE	SOURCE	IDENTIFIER
Antibodies		
Rat Anti-Mouse CD3 (clone KT3)	Abcam	Cat#ab33429, RRID:AB_726330
Rat Anti-Mouse CD68 (Clone FA-11)	Bio-Rad	Cat#ab955, RRID:AB_307338
Rat Anti-Mouse CD45 (clone 30-F11)	BioLegend	Cat#103106, RRID:AB_312971
Chicken Anti-Mouse GFP (polyclonal)	Abcam	Cat#ab13970, RRID:AB_300798
Goat Anti-Mouse CD13 (polyclonal)	R&D Systems	Cat#AF2335, RRID:AB_2227288
Rabbit Anti-Mouse P2YR12 (polyclonal)	Anawa	Cat#AS-55043A
Rat Anti-Mouse ERTR7 (polyclonal)	BioTechne	Cat#NB100-64932, RRID:AB_963381
Chicken Anti-Mouse NF-H (polyclonal)	Novus Biologicals	Cat#NB 300-217, RRID:AB_350531
Goat Anti-Mouse CD31 (polyclonal)	R&D Systems	Cat#AF806, RRID:AB_355617
Rat Anti-Mouse Ki67 (clone 11F6)	Thermo Fisher Scientific	Cat#17-5698-82, RRID:AB_2688057
Rabbit Anti-Mouse Col I (polyclonal)	Abcam	Cat#ab34710, RRID:AB_731684
Mouse Anti-Mouse alpha-SMA. (clone 1A4)	Abcam	Cat#ab184675, RRID:AB_2832195
Rat Anti-Mouse TNC (clone MTn-12)	Thermo Fisher Scientific	Cat#ma1-26778, RRID:AB_2256026
Rabbit Anti-Mouse S100b (clone EP1576Y)	Abcam	Cat#ab52642, RRID:AB_882426
Goat Anti-Mouse S100A8 (polyclonal)	R&D Systems	Cat#AF3059, RRID:AB_2184254
Chicken Anti-Mouse GFAP (polyclonal)	Abcam	Cat#ab7260, RRID:AB_305808
Mouse Anti-Human CD68 (clone KP1)	Abcam	Cat# ab955, RRID:AB_307338
Goat Anti-Human Olig2 (polyclonal)	R&D Systems	Cat#AF2418, RRID:AB_2157554
Mouse Anti-Human CD3 (clone UCHT1)	BioLegend	Cat#300406; RRID:AB_314060
Goat Anti-Human Sox2 (polyclonal)	R&D Systems	Cat#AF2018, RRID:AB_355110
Rabbit Anti-Human Collagen III (polyclonal)	Abcam	Cat#ab7778, RRID:AB_306066
Rabbit Anti-Human Collagen IV (polyclonal)	Abcam	Cat#ab6586, RRID:305584
Rabbit Anti-Human PDGFRb (clone Y92)	Abcam	Cat#ab32570, RRID:AB_777165
Goat Anti-Human GFAP (polyclonal)	Abcam	Cat#ab53554, RRID:AB_880202
Goat Anti-Human CD45 (polyclonal)	LSBio	Cat#LS-B14248, RRID:AB_2889893
Mouse Anti-Human CD8 (clone 4B11)	Bio-Rad	Cat#MCA1817T, RRID:AB_323534
Rabbit Anti-Human pan-Cadherin (polyclonal)	Abcam	Cat#ab16505, RRID:AB_443397
Rabbit Anti-Human NeuN (clone EPR12763)	Abcam	Cat#ab177487, RRID:AB_2532109
Sheep Anti-Human CD31 (polyclonal)	R&D Systems	Cat#AF806; RRID: AB_355617
Mouse Anti-Human CD15 (clone MMA)	Abcam	Cat#ab17080, RRID:AB_443635
Donkey Anti-Rat Alexa Fluor 750	Abcam	Cat#ab175750
Donkey Anti-Chicken Alexa Fluor 488	Jackson ImmunoResearch	Cat#703-545-155
Donkey Anti-Goat Alexa Fluor 750	Abcam	Cat#ab175744
Donkey Anti-Rabbit Alexa Fluor 555	Thermo Fischer Scientific	Cat#A-31572
Donkey Anti-Rabbit Alexa Fluor 647	Thermo Fischer Scientific	Cat#A-31573
Donkey Anti-Rat Alexa Fluor 555	Abcam	Cat#ab150154
Donkey Anti-Goat Alexa Fluor 555	Thermo Fischer Scientific	Cat#A-214342
Donkey Anti-Mouse Alexa Fluor 750	Thermo Fischer Scientific	Cat#A-21202
Donkey Anti-Goat Alexa Fluor 647	Thermo Fischer Scientific	Cat#A-21447
Donkey Anti-Mouse Alexa Fluor 647	Thermo Fischer Scientific	Cat#A-31571
Donkey Anti-Rabbit Alexa Fluor 488	Thermo Fischer Scientific	Cat#A-21206
Donkey Anti-Mouse Alexa Fluor 555	Thermo Fischer Scientific	Cat#A-31570

(*Continued on next page*)

Continued

REAGENT or RESOURCE	SOURCE	IDENTIFIER
Bacterial and virus strains		
LVRshp53 s generation lentivirus	In house	Chryplewicz et al.[29]
Biological samples		
Formalin-fixed paraffin-embedded primary and recurrent patient glioblastoma samples	This study	NA
Chemicals, peptides, and recombinant proteins		
SlowFade Diamond Antifade Mountant	Thermo Fischer Scientific	Cat#S36963
DAPI	Thermo Fischer Scientific	Cat#D1306
Normal Donkey Serum	Sigma-Aldrich	Cat#566460
Tris(2-carboxyethyl)phosphine hydrochloride)	Sigma-Aldrich	Cat#C4706
Guanidine Hydrochloride	Sigma-Aldrich	Cat#G3272
Urea	Sigma-Aldrich	Cat#U5378
L-Glycine	Sigma-Aldrich	Cat#G7126
Maleimide	Sigma-Aldrich	Cat#129585
Ammonium chloride	Sigma-Aldrich	Cat#A9434
Paraformaldehyde	Electron Microscopy Sciences	Cat#15714-S
Optimal Cutting Temperature (OCT) compound	Tissue-Tek	Cat#4583
Captisol Research Grade	Captisol	Cat#RC-0C7-K01
Pentobarbitol	CHUV Lausanne	
Collagenase/dispase	Sigma-Aldrich	Cat#10269638001
Fetal Bovine Serum	Fisher Scientific	Gibco™ A5256801
Myelin Removal Beads II	Miltenyi Biotec	Cat#130-096-433
Benzonase	Merck	Cat#70746
Trypsin/LysC	Promega	Cat#V5073
Critical commercial assays		
Chromium Next GEM Chip G Single Cell Kit, 16 rxns	10× Genomics	1000127
Xenium *In Situ*	10× Genomics	1000481
Xenium Mouse Brain Gene Panel	10× Genomics	1000462
Deposited data		
Mass Spectrometry Proteomic Data	Proteomexchange	Project Name: Fibrotic Response to anti-CSF-1R Treatment Potentiates Glioblastoma Recurrence Project accession: PXD041689
Single Cell RNAseq FASTQ Files	Gene Expression Omnibus (GEO)	GEO accession: GSE229409
Xenium Spatial Transcriptomic Data	Gene Expression Omnibus (GEO)	GEO accession: GSE266969
Merged Single Cell RNA-seq and Xenium Spatial Transcriptomic Data	Gene Expression Omnibus (GEO)	GEO accession: GSE266971
Experimental models: Cell lines		
GL261	NA	CVCL_Y003
DF1 chicken fibroblasts	ATCC	CRL-12203
Experimental models: Organisms/strains		
C57Bl6/J	Charles River	NA
Tg(NESTVA)J12Ech/Cdkn2a^{tm1Rdp}/J	Prof. Eric Holland	NA
FVB/N	Charles River	NA
Software and algorithms		
Zeiss Zen blue	Zeiss	Ver. 3.6.095
QuPath	Bankhead et al.	Ver. 0.3.2

(*Continued on next page*)

Continued

REAGENT or RESOURCE	SOURCE	IDENTIFIER
StarDist	Schmidt et al.	NA
HIFI Alignment Tool	Watson et al.	Ver. 0.2
R version 4.2.1	R Foundation for Statistical Computing	NA
imcRtools R Package	Eling et al.	Ver. 1.0.2
igraph R Package	Csárdi et al.	Ver. 1.3.5
nichenetr R package	Browaeys et al.	Ver. 1.1.0
GraphPad Prism	GraphPad Software	Ver. 9.4.1
Cell Ranger	10× Genomics	Ver. 6.0.1
Cytoscape	Cytoscape	Ver. 3.8.0
Xenium Ranger	10× Genomics	Ver. 2.0

EXPERIMENTAL MODELS AND STUDY PARTICIPANT DETAILS

Experimental mouse models

All animal studies were approved by the Institutional Animal Care and Use Committees of the University of Lausanne and Canton Vaud, Switzerland (License numbers: VD3804). Mice were housed in the Agora *In Vivo* Center (AIVC) animal facility in individually ventilated cages, under a 12h light/dark schedule at 22°C and in the presence of 2–4 cage mates. Standard autoclaved lab diet and water were provided *ad libitum*. The maximum humane endpoint tumor size approved per our animal protocols was 150 mm^3 for all tumor models employed.

PDG

The Nestin-Tv-a; Ink4a/Arf−/− mouse line was generously provided by Dr. Eric Holland. The mice were bred to a C57BL/6J background for 10 generations in the Joyce lab. Even distribution of mouse sex was incorporated into each experimental design. Nestin-Tv-a;*Ink4a/Arf*$^{-/-}$ mice were bred and maintained at the Agora Cancer Research Center, University of Lausanne (UNIL), Switzerland. Murine genetically engineered mouse models (GEMMs) of glioblastoma were generated as previously reported.[22,23,62,66] Briefly, 4- to 6-week-old mice were intracranially injected with DF1 cells as previously described.[10,22,23,64] Mice were fully anesthetized using isoflurane inhalation anesthesia (2% isoflurane/O_2 mixture), and a mixture of 2% lidocaine (Streuli Pharma) and 0.5% bupivacaine (Carbostesin; Aspen Pharma Schweiz) was applied as a local anesthetic (50 mL per mouse), and 0.02 mg/mL buprenorphine (Temgesic; Indivior Schweiz) was given subcutaneously as a systemic anesthetic (100 mL per mouse). Using a stereotactic apparatus, cells were injected into the right frontal cortex (2 mm frontal, 1.5 mm lateral from bregma, 2 mm deep). Nestin-Tv-a; Ink4a/Arf−/− mice were injected with 200,000 PDGFB-HA or PDGFB-HA-SV40-GFP DF1 cells (in 2 μL) and C57BL/6J mice with 40,000 GL261 cells (in 1 μL). The skin incision was sealed with Vetbond tissue adhesive (3M), and the mouse was placed on a heating pad and monitored until fully recovered from anesthesia. Finally, Bepanthen cream (Bayer) was applied on the incision site before placing the animal back in the cage, and each mouse was subsequently followed by regular monitoring.

HRas-GFAP-Cre

The initiation of LVRshp53 gliomas has been previously described.[29] Briefly, and even mix of male and female FVB/NJ-GFAP-Cre mice aged 8–12 weeks were intracranially injected with the pTomo HRasV12-Luc-shp53 lentivirus. This injection was conducted using a stereotactic frame while the mice were under full anesthesia induced by a combination of Fentanyl, Midazolam, and Medetomidine. The injections targeted the hippocampus, with coordinates set at 2.0 mm anterior/posterior, 1.5 mm medial/lateral, and 2.3 mm dorsal/ventral from the bregma. A small volume of the virus (0.8 μL, containing 1×10^8 international units) was infused at a rate of 0.1 μL/min using an automatic pump. Following the procedure, animals were revived from anesthesia with a mixture of Naloxone, Flumazenil, and Atipamezole.

GL261

Female C57BL/6J mice were injected orthotopically by intracranial delivery of 200,000 cells at matched age and cranial coordinates for tumor initiation in the PDG model.

All mice were monitored biweekly with T2-weighted 1H MRI scans on a 3T MRI machine (Bruker) and enrolled in preclinical trials when the tumors reached predetermined volumes.

Cells

DF1 chicken fibroblasts were obtained from the ATCC. RCAS virus vectors expressing PDGFB-HA or PDGFB-HA-SV40-GFP were kindly provided by Dr. Tatsuya Ozawa and Dr. Eric Holland.[53,63] DF1 cells were transfected with the RCAS vectors using FuGENE 6 (Promega) according to the manufacturer's instructions. PDGFB-HA-SV40-GFP DF1 cells were sorted for GFP-positive cells by flow cytometry to create a stable GFP-positive DF1 cell line. GL261 murine glioma cells were kindly provided by Dr. Sal Coniglio and Dr. Jeff Segall. All cell lines were cultured in DMEM (Life Technologies) supplemented with 10% fetal bovine serum (Life Technologies), and penicillin and streptomycin (Life Technologies) under standard conditions.

Patient samples

Patient tissue samples collected through the CHUV hospital were in strict compliance with the Canton of Vaud and Swiss Federal requirements for patient privacy and confidentiality. All tumor samples were surgically resected from patients with primary or recurrent glioblastoma, unless otherwise indicated. No filtering criteria were applied to CHUV patient samples, as such they represent the patient diversity treated at the CHUV hospital. Primary and recurrent glioblastoma samples from the Department of Neurosurgery at Haaglanden Medical Center/Leiden University Medical Center were provided by Dr. Marike Broekman, and were collected in strict compliance with the biobank regulations at Haaglanden Medical Center/Leiden University Medical Center and The Netherlands' rules on patient privacy and confidentiality. All patient glioblastoma samples were embedded as formalin-fixed paraffin-embedded (FFPE) blocks and sectioned onto Fisherbrand Superfrost Plus slides at 5 μm thickness prior to staining and imaging experiments.

METHOD DETAILS

Magnetic resonance imaging (MRI) of mouse glioblastoma models

MR imaging was performed using a 3 Tesla small animal MR scanner (Bruker BioSpin MRI, Ettlingen, Germany) with an 82-mm volume coil as transmitter combined with a 2 × 2 mouse brain phased array surface coil for signal reception. The mouse was fully anesthetized with 1–2% isoflurane/oxygen inhalation and placed on the imaging bed with the head held in place below the surface coil, while monitoring respiratory rate and temperature. Data acquisition was performed using the Paravision 360 v2.0 software (Bruker BioSpin MRI, Ettlingen, Germany). A 3-slice localizer was performed to assess the mouse head position. 2D turbo rapid acquisition relaxation enhancement (Turbo-RARE) T2-weighted acquisition was performed with the following pulse sequence parameters: TR = 3000 ms, TE = 75 ms, NA = 6, number of slices 10, slice thickness (ST) = 0.7 mm, FOV = 20 × 20 mm^2, pixel size 0.156 × 0.156 mm^2, (ETL = 12, T_{acq} = 3 min) with images being acquired in axial planes. After imaging, the mouse was returned to the cage and monitored until it regained consciousness. Volumetric analysis of the tumors was performed on MRI DICOM files using the MIPAV software (National Institutes of Health, USA).

Production and titration of lentiviral particles

High-titer lentiviral particles were generated following the method described by Salmon and Trono (2006). Initially, HEK293T cells were plated at 9 × 10^6 cells per 15-cm dish one day prior to transfection. The transfection mix for each dish was prepared by combining 22.5 μg of the transfer vector plasmid (supplied by I. Verma, pTomo H-rasV12-shp53-Luc), 7.9 μg of pMD2G (Addgene, 12259), and 14.6 μg of pCMVR8.74 (Addgene, 22036) with 0.66 mL of 0.1× TE buffer, 0.35 mL of distilled water, 113 μL of 2.5M CaCl2, and 1.14 mL of 2× HeBS. The resulting precipitate was added gradually to the cells and incubation continued overnight. The following day, the medium was refreshed, and the viral particles were harvested over three to four 12-h periods. The collected supernatants were pooled, filtered through a 0.22 μm filter, and concentrated by ultracentrifugation at 25,000 rpm using a Hitachi CP100NX ultracentrifuge. The concentrated viral particles were resuspended in PBS and stored at −80°C.[65]

Ionizing radiotherapy treatment

Mice with PDG tumors exceeding 30 mm^3, HRas-GFAP-Cre tumors exceeding 20 mm^3, or GL261 tumors exceeding 20 mm^3 were anesthetized by isoflurane and administered a single whole-brain focalized 10 Gy dose of ionizing radiation using the Precision X-ray X-RAD SmART irradiator. MRI monitoring was continued following IR treatment, and mice were euthanized at experimental time points as approved by the Institutional Animal Care and Use Committee.

Surgical tumor resection

Mice with tumors approximately 20 mm^3 were anesthetized by isoflurane, then craniums were exposed by scalpel incision, followed by MRI-guided craniotomy with a 2 mm biopsy punch. Partial resection was performed with a 2 mm biopsy punch lowered 2.5 mm into the brain, followed by margin aspiration with sterile glass pipets.[67] NeuroPatch (Braun) was used to seal craniotomies, VetBond (3M) was used to seal scalp incisions, and mice were monitored for tumor recurrence by MRI, and euthanized at experimental time points as approved by the Institutional Animal Care and Use Committee.

Multidrug treatments

BLZ945 (Novartis) was prepared at a 12.5 mg/mL concentration in 20% Captisol/sterile H_2O. Mice received 200 mg/kg by daily oral gavage. Dexamethasone sodium phosphate (Selleckchem) was prepared in 0.4 mg/mL, 0.2 mg/mL, and 0.1 mg/mL concentrations in sterile saline. Mice received 1 mg/kg intraperitoneal (IP) injections of 0.4 mg/mL DEX twice daily for the first 14 days of treatment trials. Mice were then tapered off DEX treatment by receiving 0.5 mg/kg IP injections of 0.2 mg/mL DEX for 7 days, then 0.025 mg/kg IP injections of 0.1 mg/mL DEX. Galunisertib (Selleckchem) was prepared at a 5 mg/mL concentration 20% Captisol/sterile H_2O. Mice received a daily dose of 50 mg/kg GAL by oral gavage for the first 10 days of treatment trials. Mice under treatment were monitored biweekly by MRI for signs of tumor recurrence. Mice in survival trials were treated until the 16-week endpoint, or when tumor recurrence exceeded double the volume of the dormant lesion, then euthanized for tissue harvest. Additionally, tissues for experimental time points were collected by euthanizing mice at predetermined days post-treatment as approved by the Institutional Animal Care and Use Committee.

Animal euthanasia and tissue collection were performed by pentobarbital injection, followed by intracardiac perfusion with 10 mL of PBS, followed by 10 mL of PLP buffer. PLP buffer consisted of 1% paraformaldehyde (PFA), 0.2% NaIO4, 37.5% L-lysine and 37.5% P-buffer (containing 81% of Na_2HPO_4, 19% of NaH_2PO_4 diluted in water, pH = 7.4) (Sigma Aldrich). Brains were harvested and fixed in PLP overnight at 4°C with gentle shaking. Tissue samples were washed in PBS, then transferred to 30% sucrose overnight at 4°C with gentle shaking. Finally, mouse brains were flash-embedded in Optimal Cutting Temperature (OCT) compound (Tissue-Tek), then cryosectioned onto Fisherbrand Superfrost Plus slides at 10 μm thickness. All slides were stored at −80°C until used for staining and imaging experiments.

Hyperplexed Immunofluorescence Imaging and spatial analysis

HIFI was performed as previously reported.[30] Cryosectioned tissue slides were thawed at room temperature (RT) and allowed to dry for 15 min, then OCT was removed in a PBS bath at RT for 5 min with gentle agitation. Post-fixation was performed in 4% PFA on ice for 5 min, followed 2× 5-min PBS washes and quenching in 0.1 M glycine for 20 min at RT. Dewaxing and antigen retrieval in pH 9.0 EDTA buffer was performed for FFPE sections. Slides were placed into humidified chambers, and tissue sections were outlined with a hydrophobic barrier using peroxidase-*anti*-peroxidase (PAP) pens. Sections were permeabilized with 0.2% Triton X-100 in PBS for 10 min at RT, then washed twice in PBS at RT with gentle agitation.

A panel of 16 antibodies was generated for cell types and ECM proteins of interest (Table S1). Multiple protein targets derived from proteomic analysis were tested for each cell type and extracellular structure, and the most highly conserved and representative markers were chosen for inclusion in the multiplexed staining panel. Specific ECM markers were selected for their ability to spatially define regions of fibrosis, focusing only on the most consistently expressed proteins. Due to ubiquitous co-expression, collagen I, collagen IV, and fibronectin are used interchangeably to define regions of fibrosis in this study. The panel consisted of 4 sets of 4 multiplexed antibodies. Prior to the first round of antibody labeling, all slides were initially imaged with only DAPI labeling to capture the autofluorescence in each wavelength channel. Slides were stained for nucleic acid with DAPI at 1:2000 dilution in HIFI Staining Buffer (HSB; 5% normal donkey serum (Merck) and 100 mM NH_4Cl (Sigma Aldrich) in PBS) for 10 min at RT, then washed 3 times in PBS at RT with gentle agitation. SlowFade Diamond (Invitrogen) mounting medium and 22 × 22 cm glass coverslips were used to mount slides for imaging. Tissue sections were imaged at 20× magnification on a Zeiss Axio Scan Z1 tile-scanning fluorescent microscope with Colibri LED light source. Imaging channels were optimized for fluorophore emission wavelengths of 350 nm, 488 nm, 555 nm, 647 nm, and 750 nm.

Following imaging, coverslips were removed in a PBS bath with gentle agitation. Sections were blocked with HIFI Blocking Buffer (HBB; 10% normal donkey serum (Merck), 150 mM Maleimide (Sigma Aldrich), and 100 mM NH_4Cl (Sigma Aldrich) in PBS) for 1 h at RT as previously described.[68] HBB was then removed and replaced with the primary antibody mix in HSB and allowed to incubate for 1.5 h at RT on an orbital rocker. Slides were washed 3 times in PBS for 5 min at RT with gentle agitation following primary antibody incubation, then secondary antibody mix with conjugated fluorophores in HSB was added, and slides were incubated for 1 h at RT on an orbital rocker. All secondary antibodies were raised in donkey to optimize compatibility. Slides were washed 3 times in PBS for 5 min at RT with gentle agitation following secondary antibody incubation, directly conjugated antibodies in HSB were added, and slides were incubated for 1 h at RT on an orbital rocker. If no conjugated antibodies were included in that HIFI round, slides proceeded to the next step. Slides received three final washes in PBS for 5 min at RT with gentle agitation and were then mounted for imaging. Slides were again imaged with fluorescent tile-scanning at 20× magnification, and exposure times and LED power for each channel were set to experimentally predetermined settings. Following imaging of the first round of markers, coverslips were again removed, and antibodies were eluted by adding elution buffer (0.5 M Glycine, 3 M guanidine hydrochloride (Sigma Aldrich), 3 M Urea (Sigma Aldrich), 40 mM tris(2-carboxyethyl)phosphine (Sigma Aldrich), in deionized H_2O) for 3 min with gentle agitation at RT. The above process was repeated for all rounds of antibody panels.

HIFI and fluorescence image processing

Immunofluorescence image post-processing was performed using the Zeiss Zen software (Version 3). Tile stitching and fusion were performed for all images at the highest quality settings. Background subtraction was performed with the rolling-ball subtraction method using a diameter of 75 μm. If necessary, images were cropped to the area of interest. Multiple rounds of sequential immunolabeling for each sample were aligned and merged with the HIFI Alignment Tool[30] to produce a single OME.TIFF high-dimensional image.

The pre-labeling imaging step captured the autofluorescence present in each tissue. For FFPE patient samples, the 'Background Subtraction' feature of the HIFI Alignment Tool was used to subtract this autofluorescence from the tissue at a pixel-by-pixel level for all fluorescent channels.

Machine learning image segmentation and cell classification

Regional tissue annotation was performed in QuPath[69] (version 0.3.2). Binary classifiers were generated to create ROIs for the entire lesion, vessels, areas of ECM, and tumor versus surrounding parenchyma. All classifiers used the Random Forrest machine learning algorithm, full resolution, and were trained on 25% of image data. The lesion classifier was trained using all available channels, holes and fragments less than 20,000 pixels were removed from ROIs. Manual removal of tissue deformations resulting from tissue sectioning or misalignment was performed on all lesion ROIs. Vessel classifiers were trained using only CD31, CD13, and DAPI. Holes and fragments of less than 20 pixels were removed. Vessel ROIs were expanded by 15 μm to create perivascular annotations. The

ECM classifier was trained using the collagen I, CD13, and TNC channels. Holes less than 50 pixels and fragments less than 300 pixels were removed from ROIs.

Region classification for measurements of fibrosis in preclinical trial samples used DAPI, collagen IV, fibronectin, and ER-TR7 as input channels. Fragments less than 200 pixels were removed from ROIs. Positive detection of the meninges or choroid plexus unrelated to the post-treatment tumor lesion were manually removed from ROIs.

Cell segmentation was performed with the CNN-based StarDist algorithm[70] implemented in Qupath. For improved accuracy, a model for deep learning segmentation was generated using manually segmented training data from PDG sample images.[30] A probability score was generated for each nucleus predicted by StarDist to indicate nuclear segmentation confidence and used for subsequent filtering. Nuclei with probability scores less than 0.6, and areas less than 9.5 μm or greater than 90 μm were removed from data analysis. Each nucleus was expanded by 3 μm to approximate the surrounding cytoplasm. The expansion was constrained by the size of the detected nuclei, so that a cell was not larger than 1.5 times the size of its nucleus. This produced 4 measurement zones per object: nucleus only, cytoplasm only, whole cell, and cell membrane. The following measurements were taken of every single-cell object: X-Y object centroid coordinates of each nucleus; area, perimeter, and circularity of each nucleus and cell; distance of each object centroid to the nearest regional annotation border; distance of each object centroid to the nearest neighbor object of an alternate cell type; and MFI for each of the 4 measurement zones.

Cell classification was performed by generating machine learning classifiers for each cell type of interest in QuPath. Training was performed by murine glioma specialists providing manually annotation of select cell types based on the antibody marker panel. Binary object classifiers were trained using the random forest method on 25% of image data and all available markers, and validated on a separate 25% subset of image data. Object classifiers were applied sequentially to the unclassified pool of cells per image.

HIFI spatial analysis and quantification

Cell neighborhood and interaction analysis were performed in R with RStudio using the imcRtools[37] package version 1.0.2, and nearest neighbor distance network analysis used the igraph package.[71] HIFI image measurements were repackaged into SingleCellExperiment objects for analysis. An expansion radius of 30 μm was used to generate a spatial connectivity map for cells within each image, connectivity maps for all images were pooled together and clustered to identify 13 distinct cell neighborhoods. Cell object identifiers were reassigned with their respective cluster number and quantified for each image and treatment type. Interaction analysis was performed using the 'classical' method, randomly reassigning each cell type with 1000 iterations to create a null distribution pattern for the statistical comparison of significant cellular interactions within each treatment type.

Mean nearest neighbor distance measurements for each treatment type were compiled into distance matrices of mean and standard deviation, and distance networks were generated with igraph using the Fruchterman-Reingold layout algorithm to set edge lengths as proportional to the mean distance between two cell types. Edge widths were modified based on the standard deviation of the mean, such that edge width was the inverse of variability (1/SD). Edge widths below a threshold were removed from each network. The edge width threshold was determined as the median standard deviation of a network multiplied by an experientially predetermined network heterogeneity cofactor constant. Node size for each cell type was based on binned percent-total populations, so that cell type nodes with populations. Network plots were clustered (gray outlines) using Louvain clustering with a resolution of 1.1 to determine cell-type nodes with similar distance patterns.

Mass spectrometry proteomic analysis

Mice bearing PDGs >30 mm^3 in volume were treated daily with BLZ945 and euthanized at predetermined experimental time points as previously described. Brains were removed from mice following intracardiac perfusion with PBS (no fixative was used in tissue harvested for proteomic analysis). Samples were collected for untreated tumors ($n = 6$), 7 days of treatment ($n = 3$), 28 days of treatment ($n = 6$), tumors that rebounded under treatment ($n = 5$), fibrotic scars from rebound tumors ($n = 5$), and tumors that stayed regressed until the 16-week trial endpoint ($n = 3$). All brains were frozen unfixed in OCT compound, and serially sectioned. Tissues were sectioned with alternating thicknesses; 2 sections were cut at 10 μm and the third was cut at 100 μm, then repeated throughout the tissue block. For each set of 3 sections, one 10 μm section was stained with H&E, the other 10 μm stained with Picrosirius Red (PSR), and the 100 μm section was left unstained and stored at −80°C. Manual microdissection was performed on dry ice for multiple (5–8) 100 μm sections per sample using the H&E and PSR images as guides to excise areas of tumor, fibrotic scar, and contralateral healthy brain.

Pooled tissue for each spatial zone in each sample was submitted to the UNIL Protein Analysis Facility (PAF) for proteomic analysis by liquid chromatography coupled to mass spectrometry (LC-MS/MS). Samples were digested following a modified version of the iST method[72] (named miST method). Tissues were resuspended in 120 μL of miST buffer (1% sodium deoxycholate, 100 mM Tris pH 8.6, 10 mM DTT), heated at 95°C for 10 min and sonicated on a Bioruptor system for 15 min and 2 × 5 s on a tip sonicator. Based on tryptophane fluorescence quantification,[73] 20–200 μg of proteins were transferred to new tubes. Samples were diluted 1:1 (v/v) with water containing 4 mM $MgCl_2$ and benzonase (Merck #70746, 100× dil of stock = 250 units/μL), and incubated for 15 min at RT to digest nucleic acids. Reduced disulfides were alkylated by adding ¼ vol. of 160 mM chloroacetamide (32 mM final) and incubated for 45 min at RT in the dark. Samples were adjusted to 3 mM EDTA and digested with 2 μg Trypsin/LysC mix (Promega #V5073) for 1 h at 37°C, followed by a second identical digestion step. Digests were desalted on a strong cation exchange (SCX) plate (Oasis MCX; Waters Corp. #186001830BA) by centrifugation. After washing with isopropanol/1% TFA, peptides were eluted in 200 μL of

80% MeCN, 19% water, 1% (v/v) ammonia, and dried by centrifugal evaporation. Peptides were redissolved in 2% acetonitrile, 0.05% TFA for LC-MS analysis in variable volumes to compensate for differences in amount based on protein quantitation.

Data-dependent LC-MS/MS analyses of samples were carried out on a Fusion Tribrid Orbitrap mass spectrometer (Thermo Fisher Scientific) interfaced through a nano-electrospray ion source to an Ultimate 3000 RSLCnano HPLC system (Dionex). Peptides equivalent to 1 μg of digested protein were separated on a reversed-phase custom packed 45 cm C18 column (75 μm ID, 100 Å, Reprosil Pur 1.9 μm particles, Dr. Maisch, Germany) with a 4–90% acetonitrile gradient in 0.1% formic acid (total time 140 min). Full MS survey scans were performed at 120,000 resolution. A data-dependent acquisition method controlled by Xcalibur software (Thermo Fisher Scientific) was used that optimized the number of precursors selected (''top speed'') of charge 2+ to 5+ while maintaining a fixed scan cycle of 0.6 s. Peptides were fragmented by higher energy collision dissociation (HCD) with a normalized energy of 32%. The precursor isolation window used was 1.6 Th, and the MS2 scans were done in the ion trap. The m/z of fragmented precursors was then dynamically excluded from selection during 60 s. An aliquot of all samples was injected the first time for a survey analysis on a short 40-min LC method (data not shown). Data were analyzed by MaxQuant and total intensities obtained were used to adjust injection volumes in long gradient analyses to compensate for remaining differences in total protein loading.

Data files were analyzed with MaxQuant 1.6.3.4[74] incorporating the Andromeda search engine.[75] Cysteine carbamidomethylation was selected as fixed modification while methionine oxidation and protein N-terminal acetylation were specified as variable modifications. The sequence databases used for searching were the mouse (Mus musculus) reference proteome based on the UniProt database (www.uniprot.org, version of January 31st, 2019, containing 54,211 sequences), and a ''contaminant'' database containing the most usual environmental contaminants and enzymes used for digestion (keratins, trypsin, etc.). Mass tolerance was 4.5 ppm on precursors (after recalibration) and 20 ppm on MS/MS fragments. Both peptide and protein identifications were filtered at 1% FDR relative to hits against a decoy database built by reversing protein sequences. The ''match between runs'' option was activated and the MaxLFQ algorithm was applied for quantitation.[76]

Initial processing of data was done with the Perseus software package.[77] Reverse (decoy) database hits and contaminant proteins were removed, and LFQ intensity values were log2-transformed. Data for 56 samples were retained in the final version of the analysis. The initial dataset contained 7622 protein groups. Of these, 4561 were quantified in at least 75% of all samples and were retained for further analysis. Missing values were inferred by imputation with standard Perseus parameters (width 0.3, down-shift 1.8 separately for each column), followed by row normalization using *Z* score.[78] Hierarchal clustering and principal component analysis (PCA) were performed on the protein abundance data tables. Gene set enrichment analysis (GSEA) was performed for comparisons between each sample type based on gene names for each identified protein. MSigDB databases employed were Hallmarks, Gene Ontology (GO), KEGG, REACTOME, and BioCarta. Permutation type was set to Phenotype, with 1000 permutations per analysis. GSEA results were analyzed by enrichment mapping in Cytoscape (version 3.8.0).

Single cell RNAseq analysis

PDG samples were harvested from mice with tumor volumes >30 mm^3 prior to treatment ($n = 3$), 7 days post-treatment with BLZ945 as previously described ($n = 3$), and after 14 days of treatment ($n = 4$). Mice were euthanized with pentobarbital, perfused with cold PBS, and whole brains were extracted. Tumors and treated lesions were dissected from brains and minced in cold PBS. For each sample, gentleMACS C tubes (Miltenyi Biotec) were prepared with 4.8 mL 2% FBS in PBS with 100 mg/mL collagenase/dispase (Sigma-Aldrich). Minced tissue samples were added to the gentleMACS C tubes, then incubated for 30 min at 37°C with constant low-speed rotation. Samples were then centrifuged at 300 × g for 5 min at 4°C and pellets were resuspended in 5 mL HBSS on ice. Cells were passed through a sterile 100 μm filter, centrifuged again at 300 × g for 5 min at 4°C, pellets were resuspended in myelin removal bead mixture (1800 μL FACS buffer with 200 μL myelin removal beads II (Miltenyi Biotec)), and incubated for 15 min at 4°C. 18 mL FACS buffer was added to each sample, centrifuged at 300 × g for 5 min at 4°C, resuspended in 1 mL FACS buffer, and filtered through LS columns (Miltenyi Biotec). Samples were incubated with red blood cell lysis buffer for 15 min at room temperature, then centrifuged at 300 × g for 5 min at 4°C and resuspended in 100 μm FACS buffer. Samples were incubated for 5 min at RT with DAPI and Reddot, and sorted for live cells on an Astrios cell sorter (Beckman Coulter). Subsequently, samples were processed using the Chromium Next GEM Single Cell 3′ Reagent Kits v3.1 (Dual Index, 10× Genomics). Libraries were quantified by a fluorometric method (Qubit, Thermo Fisher) and their quality was assessed on a Fragment Analyzer (Agilent Technologies) in the Lausanne Genomic Technologies Facility (GTF) operated by the University of Lausanne. Samples were sequenced by GeneWiz on the NovaSeq 6000 (Illumina).

Mapping was performed using CellRanger (version 6.0.1) with default parameters on the mouse reference transcriptome refdata-gex-mm10-2020-A complemented with the following 2 sequences.

Transgene 1: eGFP

CATGGTGAGCAAGGGCGAGGAGCTGTTCACCGGGGTGGTGCCCATCCTGGTCGAGCTGGACGGCGACGTAAACGGCCACAAGT
TCAGCGTGTCCGGCGAGGGCGAGGGCGATGCCACCTACGGCAAGCTGACCCTGAAGTTCATCTGCACCACCGGCAAGCTGCCC
GTGCCCTGGCCCACCCTCGTGACCACCCTGACCTACGGCGTGCAGTGCTTCAGCCGCTACCCCGACCACATGAAGCAGCACGAC
TTCTTCAAGTCCGCCATGCCCGAAGGCTACGTCCAGGAGCGCACCATCTTCTTCAAGGACGACGGCAACTACAAGACCCGCGCCG
AGGTGAAGTTCGAGGGCGACACCCTGGTGAACCGCATCGAGCTGAAGGGCATCGACTTCAAGGAGGACGGCAACATCCTGGGGC
ACAAGCTGGAGTACAACTACAACAGCCACAACGTCTATATCATGGCCGACAAGCAGAAGAA.

CGGCATCAAGGTGAACTTCAAGATCCGCCACAACATCGAGGACGGCAGCGTGCAGCTCGCCGACCACTACCAGCAGAACACC
CCCATCGGCGACGGCCCCGTGCTGCTGCCCGACAACCACTACCTGAGCACCCAGTCCGCCCTGAGCAAAGACCCCAACGAGAA
GCGCGATCACATGGTCCTGCTGGAGTTCGTGACCGCCGCCGGGATCACTCTCGGCATGGACGAGCTGTACAAGTA.

Transgene 2: hPDGFB

ATGAATCGCTGCTGGGCGCTCTTCCTGTCTCTCTGCTGCTACCTGCGTCTGGTCAGCGCCGAGGGGGACCCCATTCCCGAGGAG
CTTTATGAGATGCTGAGTGACCACTCGATCCGCTCCTTTGATGATCTCCAACGCCTGCTGCACGGAGACCCCGGAGAGGAAGATG
GGGCCGAGTTGGACCTGAACATGACCCGCTCCCACTCTGGAGGCGAGCTGGAGAGCTTGGCTCGTGGAAGAAGGAGCCTGGGT
TCCCTGACCATTGCTGAGCCGGCCATGATCGCCGAGTGCAAGACGCGCACCGAGGTGTTCGAGATCTCCCGGCGCCTCATAGAC
CGCACCAACGCCAACTTCCTGGTGTGGCCGCCCTGTGTGGAGGTGCAGCGCTGCTCCGGCTGCTGCAACAACCGCAACGTGCAG
TGCCGCCCCACCCAGGTGCAGCTGCGACCTGTCCAGGTGAGAAAGATCGAGATTGTGCGG.

AAGAAGCCAATCTTTAAGAAGGCCACGGTGACGCTGGAAGACCACCTGGCATGCAAGTGTGAGACAGTGGCAGCTGCACGGCC
TGTGACCCGAAGCCCGGGGGGTTCCCAGGAGCAGCGAGCCAAAACGCCCCAAACTCGGGTGACCATTCGGACGGTGCGAGTCC
GCCGGCCCCCCAAGGGCAAGCACCGGAAATTCAAGCACACGCATGACAAGACGGCACTGAAGGAGACCCTTGGAGCCGCCTAC
CCTTATGACGTGCCAGATTATGCCTAG.

Counts matrices were imported into R (version 4.0.3) and subsequently analyzed using the Seurat package (version 4.3.0). The count matrix was filtered to retain the following: cells bearing between 200 and 7,500 genes, cells bearing with less than 10% of mitochondrial gene counts, and genes detected in at least 5 cells.

Doublet prediction was performed per sample using DoubletFinder (version 2.0.3). PC neighborhood sizes (pK) were set to the maximum mean-variance normalized bimodality coefficient (BCmvn), and the pANN threshold (nExp) was set to 2.5%, 859 cells identified as doublets were filtered out, resulting in a final set of 37,300 cells and 21,979 genes. Gene counts were normalized using regularized negative binomial regression for data normalization and variance stabilization, SCTransform (version 0.3.5). The percentage of mitochondrial genes was used to regress out in a second non-regularized linear regression.

PCA was computed with the RunPCA function using 3000 most variable features and unsupervised cell clustering was performed applying the graph-based clustering approach and Louvain algorithm implemented in the Seurat R package, with the distance metric which drives the clustering analysis based on previously identified 30 PCs. Uniform Manifold Approximation and Projection (UMAP) dimensionality reduction was derived through the RunUMAP function based on the first 30 PCs. Marker genes were computed using FindAllMarkers function, using the parameters min.pct = 0.25 and only.pos = TRUE, and used to identify clusters as cell populations.

Differential expression was computed on genes that are expressed in at least 10% of the cells of a given population, in at least one sample of the 3 sample groups and with average logCPM >5. Genes differentially expressed between clusters were determined using the pseudobulk approach of edgeR implemented in muscat (version 1.4.0) after gene counts were aggregated by their sum per sample and cluster with the function aggregateData. Genes with an FC > 1.5 or < −1.5 and adjusted p-value <0.05 were kept for the ORA analysis, executed through clusterProfiler (version 3.18.1). GSEA was also performed on the full list of genes ranked, using KEGG, Hallmark and Reactome collections of msigdbr (version 7.5.1).

T cell subtype analysis was performed with the R package ProjecTILs.[45] Briefly, the expression matrix was filtered to keep only T cells and was projected on the precomputed a cross-study pan-cancer murine TIL Atlas version 1.0 (http://tilatlas.unil.ch/) based on 16,803 high-quality single-cell transcriptomes from 25 samples (B16 melanoma and MC38 colon adenocarcinoma tumors) from six different studies (available at https://doi.org/10.6084/m9.figshare.12478571, and interactively at https://spica.unil.ch/refs/TIL). Pre-filtering of T cells (filter.cells option) and log-normalization of counts (skip.normalize option) were not performed. The prediction of cell states was performed using a nearest-neighbor algorithm (dedicated R functions with default parameters).

Spatial transcriptomic analysis

Gene panel design and probe hybridization

We employed the Xenium *In Situ* technology platform (10× Genomics) to detect gene expression in murine brain tumor samples. Our customized gene panel was based on the standard Xenium Mouse Brain Panel and included an additional 100 genes selected from single-cell RNAseq data of replicate samples. This panel featured 347 genes optimized for cell type identification and phenotypic interrogation, including custom probes for eGFP and human-PDGFB transgenes.

Sample preparation and imaging

Fixed-frozen mouse brain sections were prepared at 8 μm thickness, mounted on Xenium slides, and processed through fixation and permeabilization steps. 6-7 separate mouse tumor samples were placed in the analysis window of each Xenium slide. We hybridized tissue sections with the customized 347-gene panel probes, maintaining stringent conditions to minimize non-specific binding. After overnight hybridization at 50°C and subsequent stringent washes, probes were ligated and amplified using a rolling circle amplification strategy. All tissue sections were subsequently imaged on the Xenium Analyzer v1.7.

Image acquisition and processing

The analyzer conducted 15 rounds of fluorescent probe hybridization and imaging, with a z-step resolution of 0.75 μm to comprehensively cover the tissue thickness. The captured z-stacks were processed to stitch together a comprehensive spatial map of gene expression, employing puncta detection algorithms to localize mRNA molecules precisely. Each detected transcript was decoded based on its unique optical signature and assigned a quality score (Q-score) to ensure accurate identification. Transcripts with a Q-score of 20 or higher were used for further analysis.

Protein labeling and cell segmentation

Following image acquisition, slides were further processed for HIFI-based detection of 16 proteins. Each round of protein labeling was corrected for pixel scale and aligned to the DAPI images acquired on the Xenium Analyzer for each sample. We employed the iMAXT StarDist nucleus detection model on HIFI images in QuPath for cell segmentation.[30,69,70] Protein MFIs were measured for each cell in each sample in QuPath, and cell segmentation objects were exported to Xenium images using Xenium Ranger, and nuclear objects were expanded by 5 μm to capture cytoplasmic RNA expression. The spatial distribution of mRNAs was mapped to within cellular boundaries for downstream analysis.

Integrated spatial transcriptomic analysis

Preprocessing of the spatial transcriptomics data

The output files from Xenium Ranger were loaded into R and used to create a Seurat spatial transcriptomics object (one per sample) using the LoadXenium function (Seurat package, verison 5.0.1). Cells with zero counts across all mRNAs were discarded. Normalization and variance stabilization was performed using the SCTransform function.

Integration of the Xenium and HIFI data (protein MFIs and distances to fibrotic niches)

To match cells from Xenium and HIFI data corresponding to the same tissue section, we applied a fast nearest neighbor search algorithm on the 0–1 scaled coordinates of the cellular centroids, using the get.knn function from the FNN R package (version 1.1.4). Xenium cells that matched to the same HIFI cell as other Xenium cells, and Xenium cells that were too distant from their nearest HIFI cell (cutoff based on an outlier analysis of distances using the boxplot.stats R function), were discarded.

Projection of cell population identities from the single cell RNA sequencing data onto the Xenium data

The single cell RNA sequencing data was used as a reference (all time points pooled) to project cell population identities onto the Xenium spatial data. Projection was performed following the standard Seurat procedure for data transfer (FindTransferAnchors and TransferData functions) with reference.reduction set to "pca", dims set to "1:30", and other parameters set to the default values. Only cells with a cell population identity score ≥ 0.8 were annotated.

Cell population identification

Cells were split by sample according to their distance to the nearest fibrotic region ("inside the fibrotic niche" if distance ≤ 5 μm, "outside the fibrotic niche" otherwise). PCA of the split data was performed using the RunPCA function and the first 30 principal components were used for nearest-neighbor graph construction (FindNeighbors function) and UMAP non-linear dimensionality reduction (RunUMAP function). Unsupervised clustering was performed using a shared nearest neighbor modularity optimization algorithm (FindClusters function), with the resolution adjusted for aiming at around 30 clusters. Clusters were manually annotated with their inferred cell population by considering the HIFI protein MFIs (trimmed at the 0.99 percentile and 0–1 scaled), cell population identities projected from the single cell data, and signature scores from manually curated sets of Xenium panel genes (Supplemental table "Supp_Xenium_signatures.xls"). Signature scores were computed using the AddModuleScore_Ucell function from the Seurat R package, which uses the Mann-Whitney U statistic from the UCell R package (version 2.4.0). To better identify lymphocytes and neutrophils, for which there was a low number of markers in the Xenium panel and no HIFI associated proteins, we excluded the neuronal cells and their associated genes from the annotated data and repeated the dimensionality reduction and unsupervised clustering procedures.

Splitting rebound tumor cells into zones

Cells were split into four concentric zones according to the quartiles of the distribution of distances from treatment-associated fibrotic niche.

Differential gene expression analyses

Xenium transcriptomic data from different time points and fibrosis association compartments were integrated using the STACAS R package (version 2.2.2) semi-supervised method (taking cell populations identities into account for guiding the alignment of the transcriptional profiles). Analyses of differential gene expression between groups of cells were performed using the FindMarkers function from Seurat. Genes with an absolute average log2 fold-change >1 and adjusted p-value <0.05 were considered as significantly differentially expressed.

T cell exhaustion signature scores

Scores were computed using the AddModuleScore_UCell function and the signature was composed of the *Ctla4*, *Lag3*, *Pdcd1* and *Tigit* genes.

Intercellular communication analysis of scRNA-seq data with integrated spatial colocalization data derived from HIFI

We adapted the NicheNet method,[46] implemented in the nichenetr R package (v1.1.0), by incorporating probabilities of cell-to-cell communication inferred from spatial data.[79] The NicheNet method is aimed at predicting which ligands from one or more sender cell populations are most likely to affect target gene expression in interacting receiver cell populations (ligand activity analysis), and which specific target genes are affected by which of these predicted ligands. In NicheNet, ligand activities can be measured by the correlation between their predicted potential to regulate target gene expression (based on a prior model of ligand-receptor-target interactions) and the observed transcriptional response. We adapted this method by using weights for this measure that reflect the probabilities of intercellular interactions inferred from cell vicinity compositions in HIFI data.

Input data

- scRNA-seq dataset (as a Seurat v3 object with processed expression data): Glioblastoma cells and corresponding immune microenvironment cells (TME) from untreated mice (“UT”) and mice treated with BLZ945 (sampled at 7 and 14 days after start of treatment, pooled - “D7_D14”). Different fibroblasts cell subpopulations were pooled into a single population. Different microglia cell subpopulations were pooled into a single population.
- HIFI spatial proteomics data: Data consisted of 4 sections per tissue × 3 replicates = 12 images per “data point” (“UT”, “D7” and “D14”), with dots corresponding to individual cells, whose coordinates (in μm) were retrieved. Cells were annotated with their inferred population.
- Prior model of ligand-receptor, receptor-target and ligand-target interactions: We used the prebuilt NicheNet ligand-target matrix ("https://zenodo.org/record/3260758/files/ligand_target_matrix.rds"), ligand-receptor network ("https://zenodo.org/record/3260758/files/lr_network.rds") and weighted integrated network ("https://zenodo.org/record/3260758/files/weighted_networks.rds"). Gene symbols were converted from human to mouse based on one-to-one orthology.

We considered the following cell populations as potential “sender” or “receiver” cell populations: $CD8^+$ T cells ("CD8_Tcells"), Microglia ("microglia"), Fibroblasts ("fibroblast-like_cells"), Monocytes/macrophages ("MonoMac"), and Endothelial cells. “Tumor” cells and “T_{reg}” were not considered for this analysis as there were no differentially expressed genes between treated and untreated mice. All interactions between cell populations were tested, except self-self (autocrine) interactions.

The target gene set of interest was restricted to extracellular matrix (ECM) genes, according to Gene Ontology term GO:0031012, that were potential targets according to the prior model. Furthermore, we only considered genes that were expressed in at least 10% of cells in receiver cell populations and were significantly differentially expressed after BLZ945 treatment (p-value ≤ 0.05, average fold change ≥ 1.5). We considered as potential ligands all genes expressed in at least 10% of cells in sender cell populations that could bind receptors expressed in the receiver cell populations, according to the prior model.

Probabilities of interaction were inferred from cell vicinities in HIFI spatial data and were used downstream as weights for ligand activity analyses. Data were first downsampled so that the fractions of cell populations per image corresponded to the predicted fractions of cells sampled in the scRNA-seq experiment. Probability weights for each sender cell population – receiver cell population interaction were computed from the frequencies of receiver cells in the vicinity (within 30 μm distance) of sender cells computed from pooled “D7” and “D14” images, using the *spatstat* R package (v2.3.4), according to the following formula:

$$W_{i,j} = \frac{F_{i,j}}{\overline{F_i}}$$

where:

$W_{i,j}$ was the probability weight of the interaction between cells from population i and cells from population j ($0 < W_{i,j} <$ *number of cell populations*),

$F_{i,j}$ was the frequency of cells from population j in the vicinity of cells from population i, and

$\overline{F_i}$ was the average frequency of all cell populations in the vicinity of cells from population i

Cell population i - cell population j specific ligand activities $L_{i,j}$ were measured by the Pearson coefficient of correlation between the ligand’s regulatory potential (according to the prior model) and the observed transcriptional response in the receiver cells. Pearson coefficients were weighted by the $W_{i,j}$ to take into account the probability of interaction between cells from population i and cells from population j. Ligand activities with $L_{i,j} \leq 0.1 \times \overline{F_i}$ were discarded, and the remaining were ranked according to $L_{i,j}$. Finally, the top 100 ranked ligand activities were selected for downstream prediction of active ligand-receptor and ligand-target interactions.

We considered receptors as active if they were considered as potential receptors of the selected ligands (according to the prior model) and were expressed in the receiver cells. We considered as active ligand-target interactions the interactions between selected ligands and the top 200 potential target genes ordered by ligand-target regulatory potential (from the prior model).

Intercellular Communication Analysis Between Sender Cells in All Spatial Regions and PDFLs in the Post-Treatment Fibrotic Niche.

Identification of the PDFL receiver cells in the scRNA-seq data

A “fibrotic niche” signature score was used to identify high resolution unsupervised PDFL clusters in the scRNA-seq data with a “fibrotic niche” profile. The signature was derived from the Xenium data and consisted of the set of differentially expressed genes between PDFLs inside and outside the fibrotic niche (absolute average log2 fold-change >1.5 and adjusted p-value <0.05). The score was computed using the AddModuleScore_UCell function.

NicheNet analysis

The NicheNet method, implemented in the nichenetR R package was used to predict the interactions between Tgfb1 or Tgfb2 (potential ligands) in PDFLs, endothelial cells, microglia or monocytes/macrophages (untreated or 7-day, all spatial regions) and all potential targets in PDFL receiver cells (7-day, in fibrotic niche). Only genes expressed in at least 1% of cells were considered for this analysis. Ligands were considered active if the Pearson correlation between their potential to regulate target gene expression (according to the prior model) and the observed transcriptional response was >0.1. The transcriptional response was derived from a differential gene expression analysis of the scRNA-seq data comparing 7-day “fibrotic niche” PDFLs and untreated “fibrotic niche” PDFLs (absolute log2 FC > 1 and adjusted p-value <0.05). The top 20 active ligand-target interactions, ranked by regulatory potential were selected.

Pathology scoring

Scoring of pathological features was performed in accordance with Canton of Vaud and Swiss federal regulations regarding patient privacy protection. Matched primary and recurrent patient FFPE samples (n = 18 for each) were sectioned at 5 μm and stained with H&E and PSR. Primary and recurrent samples were slide scanned at 20× magnification on the Zeiss Axio Scan Z1, and all identifying data was removed. Images were scored for multiple features by an expert pathologist in a double-blinded study, then rematched to patient metadata.

QUANTIFICATION AND STATISTICAL ANALYSIS

Statistical analyses were performed in R with RStudio, or in GraphPad Prism (GraphPad 9.0 software). two-way ANOVA or unpaired t-tests were used for between-group comparisons, with the level of significance defined as $p < 0.05$. Data are presented as means ± SEM. Figure asterisks correlate to p-value thresholds: ns = > 0.05, * = ≤ 0.05, ** = ≤ 0.01, *** = ≤ 0.001, **** = ≤ 0.0001. For survival curves, p-values were obtained by using the Log Rank (Mantel-Cox) test.